LA-UR 94-0370

Los Alamos National Laboratory is operated by the University of California for the United States Department of Energy under contract W-7405-ENG-36.

TITLE: EXPERIMENTAL STUDY OF HYDROVOLCANISM BY FUEL-COOLANT INTERACTION ANALOGS

AUTHOR(S): Kenneth Wohletz (EES-1), Robert McQueen (DX-10), and
Meghan Morrissey (U.S. Geological Survey, 345 Middlefield Rd., Menlo Park, CA 94025)

SUBMITTED TO: NSF/JSPS AMIGO-IMI Seminar, Santa Barbara, CA, June 8-13, 1995

Los Alamos

Los Alamos National Laboratory
Los Alamos, New Mexico 87545

FORM NO. 836R4
ST. NO. 2629 581

Highly Non-equilibrium Ultra Rapid Transient Intense Multiphase Interactions

Industrial Safety
-Nuclear
-Metals
-Cryogenics
-Paper
-Chemical Process
Volcanology
Materials Processing

Synergistic Multi-disciplinary Frontier Thermal-hydraulics

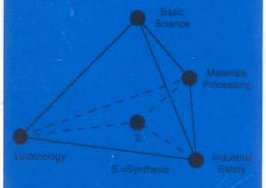

Proceedings of
US (NSF) Japan (JSPS)
Joint Seminar

A Multidisciplinary International Seminar on Intense Multiphase Interactions

June 9-13
1995
Santa Barbara

EXPERIMENTAL STUDY OF HYDROVOLCANISM BY FUEL-COOLANT INTERACTION ANALOGS

Kenneth Wohletz
Los Alamos National Laboratory
EES-1, MS D462
Los Alamos, NM 87545
(505)667-9202

Robert McQueen
Los Alamos National Laboratory
Dynamic Experimentation Division
Los Alamos, NM 87545

Meghan Morrissey
U. S. Geological Survey
345 Middlefield Rd.
Menlo Park, CA 94025
(415)329-4746

ABSTRACT

Fuel-coolant interaction (FCI) experiments with molten thermite (Al_2O_3 + Fe) in contact with water have been used to simulate hydrovolcanic eruption phenomena and allowed documentation of the controls of explosive vaporization phenomena, including kinetic energy release and melt fragmentation. In these experiments the controlling effects of water/melt mass ratio, confining pressure, and venting geometry were studied using several designs. The interaction of the hot melt with water produced a variety of phenomena from relatively passive production of steam with melt ejection to ones that must be classified as explosive. While initial designs demonstrated that these experiments could contribute substantially to our understanding of volcanic behavior, the latest experiments attempted to quantify the effects of water/melt mass ratio (R_m) and confining pressure (p_{conf}). These experiments required a high-pressure vessel to burst after a Fe-Al melt interacted with water producing a pressure pulse exceeding the strength (6 to 36 MPa) of the vessel's burst diaphragm. The conversion ratios (CR) of melt ejecta mechanical energy to thermal energy were calculated by three methods: (1) calculation of ejecta kinetic energy by analysis of ejecta photography and vessel movement records (MCR); (2) analysis of the vessel's pressure records assuming initial thermal equilibrium followed by isentropic decompression (ACR); and (3) analysis of pressure records assuming initial thermal equilibrium followed by isothermal decompression (ICR). Explosive interactions occurred at all R_m tested, including those where p_{conf} was above the critical pressure of water. Calculated MCR values ranged from 1 to 6% and are lower than those calculated from compression ratios. ACR and ICR values showed CR ranges of 3 to 14% and 5 to 29%, respectively. The values of CR show a lognormal dependence on R_m, and peak values occur where $0.3 < R_m < 1.5$. Peak values of CR increased with p_{conf}; and maximum interaction pressures exceeded 60 MPa in several experiments. Grain-size frequency distributions of sampled ejecta show finer mean values for experiments with higher CR values. We discriminated six types of ejecta grain morphologies by scanning electron microscopic digital image analysis; these morphologies have some correlation to specific combinations of R_m and p_{conf}. These results suggest that size and shape analysis of hydrovolcanic tephra provides a method for interpreting eruption conditions. Because CR values determined by measured kinetic energy (MCR) are less than ACR and ICR values (that assume initial thermal equilibrium), it is likely that the duration of these experiments (several seconds) was not long enough for close attainment of thermal equilibrium between the melt and water prior to burst. However, in volcanic systems several orders of magnitude larger in size than these experiments, time constraints for various heat-exchange processes might permit closer approach to pre-eruption thermal equilibrium.

I. INTRODUCTION

Anyone who visited Kalapana, Hawaii since 1990 most likely witnessed the spectacular activity produced by lava entering the sea and the pervasive generation of steam with the periodic explosive ejections of fragmented, incandescent lava. When Surtur crater emerged from the Atlantic ocean off the southern coast of Iceland, a vigorous up-rush of vapor and tephra was observed after seawater poured into the vent producing the famous *cock's tail* explosive jets.[1] These two volcanic events are examples of hydrovolcanism, a phenomenon caused by the physical contact of magma with external water that results in a spectrum of volcanic activity ranging from an explosive eruption of fragmented magma to the passive quenching of magma. The spectrum of activity reflects the wide variety of hydrologic environments in which magma or lava can encounter external water (*e.g.*, oceanic, lacustrine, glacial ice, phreatic), coupled with the complex heat transfer relationship between water and magma, and the degassing stage of the magma.[2]

A hydrovolcanic eruption is thought to be driven primarily by the volumetric expansion of external water after it has been rapidly heated by contact with magma; exsolving magmatic volatiles may also contribute to vapor expansion. Generally, the magnitude of a hydrovolcanic eruption depends upon the masses of water and magma interacting and the pressure driving the expansion. [3] Because an explosive event frequently results when degassed lava encounters an external source of water, many researchers have suggested that magmatic volatiles are not required to initiate a hydrovolcanic explosion. However, Barberi *et al.*[4] have argued that magmatic fragmentation prior to water interaction is necessary to allow extensive magma water mixing.

Over the past ten years a small number of experimental studies provided considerable insight on the controlling factors that may initiate an explosive hydrovolcanic eruption[2,5-9]. To minimize the contribution of primary (magmatic) vesiculation to the experimental eruption, the melt simulants used in these experiments were fairly depleted in volatiles (*e.g.*, Fe-Al thermitic melt, molten tin, and natural melts of degassed basalt and carbonatite).

The basis for these hydrovolcanic experiments stems from theoretical and experimental studies done on vapor explosions produced by the contact of hot molten metal with water, a phenomenon referred to as fuel-coolant interaction or *FCI*.[10-14] FCI refers to a heat transfer process from which vapor is generated by the interaction between a cold volatile fluid (coolant) and a hot fluid (fuel) that has a solidus temperature above the boiling temperature of the coolant.[15] The result of an FCI can be explosive or non-explosive, dependent on the rate of heat transfer between the fuel and the coolant and the subsequent pressurization rate of the coolant. An explosive FCI occurs when the rate of a local pressure rise is sufficiently high that the system cannot relieve it and the system becomes temporarily over-pressurized. The release of the over-pressure is manifested in an explosive ejection of coolant and fragmented fuel as the system decompresses to ambient conditions.[14]

The most recent experimental studies of hydrovolcanism are those of Fröhlich[7] and Zimanowski *et al.*[9], who conducted a set of hydrovolcanic experiments designed to evaluated the effect of the mode of contact of water and melt on the explosivity of the interaction. One configuration involved the entrapment of a water droplet within a pool of molten tin; a second had a layer of water resting on top of a layer of molten tin, the thickness of the water layer being varied from 1.0 to 15.0 cm. Two different events resulted from the entrapment experiment. In several experiments a thin vapor film formed between the melt and water droplet as the droplet rose through the melt pool to the free surface where it passively escaped. In the other experiments, the water droplet instantaneously vaporized as it rose through the melt pool. Upon approaching the free surface, the vapor bubble violently decompressed causing fragmentation and ejection of the constraining melt (Fig. 8 from Fröhlich[7]). Out of 100 experiments using the stratification configuration, 50 experiments produced a single explosion. Several of the experiments with water layer thicknesses greater than 10.0 cm produced multiple explosions.[7] The single explosion type of event was initiated by a steam fountain that transgressed into an energetic ejection of steam and fine-grained melt fragments. A crater formed on the melt surface coincident with the location of the explosion center. In the case of multi-explosions, the initial event was succeeded by another cratering event adjacent to the first site. The energy of the later explosions escalated as did the amount of fragmented melt. The increase in explosivity was attributed to an increase in heat flux induced by the additional surface area created by the fragmentation of melt.[7]

Zimanowski *et al.*[8] used the entrapment configuration was used to evaluate the effect of melt composition on the explosivity of the water-melt interaction. Three different melt compositions were tested, a carbonatite produced from a 1:1 mixture of Na_2CO_3 and K_2CO_3; Lengaite carbonatite; and olivine melilite. The results showed the effects of exsolution of CO_2 and viscosity on the physical interaction and subsequent explosion. The most explosive event developed from the interaction involving the synthetically produced carbonatite. Weaker explosive events were produced from the Lengaite carbonatite, the result of CO_2 exsolving during the interaction. Explosive events generated by the interaction involving a silicate melt were the least energetic. The higher viscosity of the silicate melt suppressed intermixing of the melt and water, leading to a lower heat transfer rate.

In this paper we review the evolution of our experimental progress over the past ten years with emphasis on documenting and analyzing the results of 40 of our most recent experiments. These experiments were designed to quantify the effects of the water-to-melt mass ratio and confining strength on the magnitude of experimentally produced hydrovolcanic explosions.

II. THE EXPERIMENTAL APPROACH

Our previous work[3] involved experiments designed to simulate hydromagmatic activity using an Fe-Al thermitic melt near water. A mixture of iron oxide and aluminum particles was ignited in a container to produce a molten magma simulant, which was subsequently allowed to contact and mix with water. The objectives were to monitor

dynamic events and to determine what parameters controlled the rapid conversion of the melt's thermal energy into mechanical energy when it interacted with water. The melt, simulating basaltic magma, resulted from an exothermic reaction of the fine-grained aluminum (~24 wt%) with magnetite (~76 wt%) as described by Wohletz[16]:

$$3Fe_3O_4 + 8Al = 9Fe + 4Al_2O_3 + Heat \qquad (1)$$

In general this thermite composition can be shown by consideration of heats of formation to yield about 1130 kJ excess heat per mole of iron oxide at 1800 K. In most experiments quartzo-feldspathic sand was added to the thermite at a ratio of ~1:3 to produce a silicate melt (Fig. 1; Table 1).

The physical and thermal properties of Fe-Al thermite melt are compared with those of a typical tholeiitic basaltic melt in Table 2. Using the method of Bottinga and Weil[17], which estimates viscosity of polymeric melts containing SiO_2 and Al_2O_3, viscosities in the range of about 1 to 162 Pa-s are predicted for the thermite melt at a temperature of 1800 K; the wide range reflects suspension effects of crystallites. Indeed, petrographic inspection of quenched samples of this melt revealed abundant crystallites, which indicates subliquidus melt temperatures. Accordingly, 100 Pa-s (1000 poise) is considered typical of the viscosity of the thermitic melt used in the experiments. The reader is referred to Wohletz[18], and Buxton and Benedict[14], for further discussion on the thermochemical properties of the Fe-Al thermitic reaction.

Wohletz and McQueen[3] described four different designs (Fig. 2) that were employed to evaluate the effects of contact geometry, the water to melt mass ratio (R_m), and the interaction vessel's confining strength (p_{conf}) on the explosivity of the experimental hydrovolcanic eruption. In all designs the thermite was initially held above the water by an aluminum or magnesium plate and was ignited near the top to insure that it was melted before contacting the water below. The thermite was ignited by passing a large electric current through a loop of tungsten wire wrapped with magnesium foil. The four designs included the following:

(Type I) emplacement of about 10 kg of thermite in an iron pipe above a pipe containing water;

(Type II) immersion of a 0.3-m-diameter Plexiglas tube in a large Plexiglas box containing over a cubic meter of water;

(Type III) emplacement of 90 kg of thermite suspended above water by an aluminum disk in a sealed steel cylinder (0.4 m diameter by 0.8 m long) with a vent at the top designed to burst when internal pressure exceeded ~7.0 MPa; and

(Type IV) design III modified by welding a central vent pipe extending down through the thermite into the water compartment to insure that a large fraction of the melt would be ejected.

In addition to these four designs a fifth one was developed that aided us considerably in interpreting the results obtained here. It is described in a later section.

In all experiments 16 mm motion picture films were used to record the events, typically at 48 frames/s. These films, projected at one-half real time, enabled us to view in detail interesting phenomena associated with the experiments and were useful in measuring trajectory velocities of particles and other motion. In all experiments attempts were made to collect representative samples of debris.

A. Observational Results

More than one mode of melt ejection was produced from each of the four experimental designs, all of which strongly resembled natural volcanic activity[3]. Using common volcanological eruption terminology, the main experimental phenomena were:

(1) Ejection of the thermite melt in a continuous fountain of cm-sized, liquid fragments resembling Hawaiian activity;

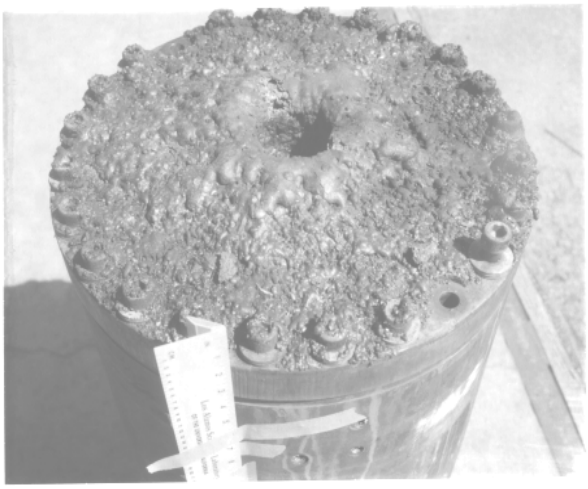

Fig. 1. Photograph of thermite flows extruded on the top surface of the experimental vessel. The surface is about 40 cm in diameter, and the vent is about 10 cm in diameter.

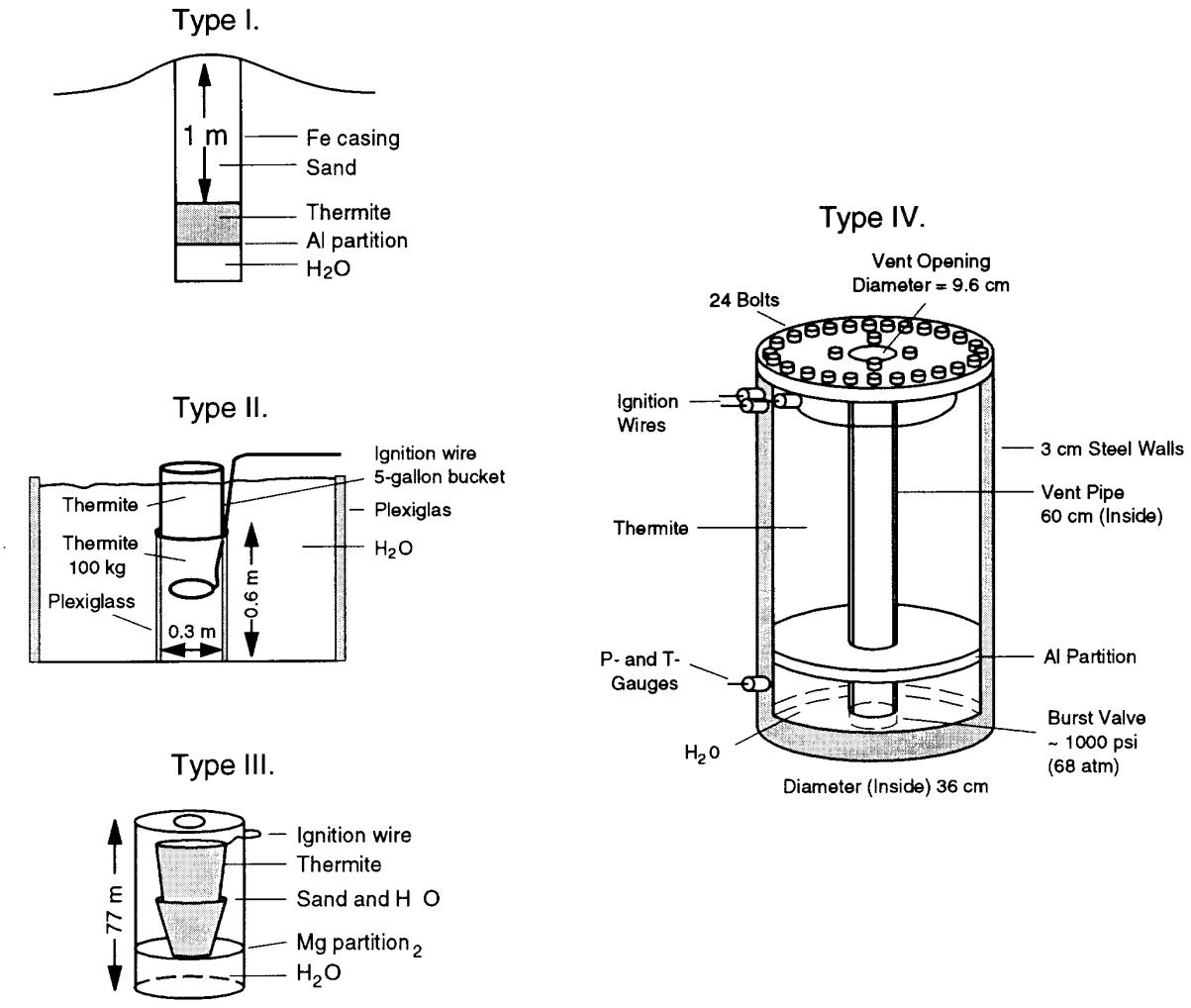

Fig. 2. Schematic diagram showing Type I through Type IV experimental designs.

Table 1. Representative Bulk Chemical Analyses in Wt% of Thermite Melt Debris*

Major Oxide	*Blocky Particle*	*Silicate Coating*	*Spindle Particle*
SiO_2	14.3	36.6	18.6
TiO_2	2.3	1.4	1.9
Al_2O_3	11.4	34.4	42.5
FeO	57.0	17.3	23.3
MnO	1.6	1.0	1.3
MgO	6.4	3.7	5.8
CaO	2.1	1.7	1.9
Na_2O	3.1	2.0	3.2
K_2O	2.0	2.0	1.9

* Standardless energy dispersive spectral analyses (EDS) with total Fe expressed as FeO

Table 2. Physical and Thermal Properties of Fe-Al Thermite and Basaltic Melt.

Properties	*Fe-Al Melt*	*Basaltic Melt*
Liquidus T	1000 - 2000 K	1370 - 1520 K
Enthalpy	3700 kJ/kg	1150 kJ/kg
Viscosity	10^2 Pa s	10^2 - 10^3 Pa s
Density	3.0 - 4.0 Mg/m^3	2.5 - 2.7 Mg/m^3
Surface Tension	0.5 N/m	0.35 N/m
Thermal Conductivity	2.4 J/(m s K)	2.1 J/(m s K)

(2) pulsating ballistic ejection of partially quenched and vesicular (scoriaceous) fragments, equivalent to Strombolian activity;

(3) dry vapor explosions propelling μm-sized dust in expanding jets of superheated steam, equivalent to strong Surtseyan activity;

(4) wet vapor bursts carrying mm-sized pellets in ballistic plumes of condensing steam, similar toe weak Surtseyan activity; and

(5) passive chilling of the thermitic melt in cm-sized masses whose surface was quenched, equivalent to submarine activity producing peperites and pillow lavas.

A more detailed description of these experiments is given in the next sections along with some pertinent observations (Table 3).

1. Type I—Small Water/Melt Ratio with No Confinement. Two experiments were designed to test the feasibility of using thermite as a magma simulant. In the first, about 27 kg of thermite were placed in an iron pipe above a container with about 5 kg of water. For the second test, 50 kg of thermite and 6.3 kg of water were used in conjunction with a vent nozzle 2/5 the diameter of the pipe holding the thermite. The second test resulted in a more vigorous eruption than the first, ejecting roughly twice as much material in about one-half the time of the first, which we attribute to the increased pressure produced by the vent nozzle. Several other similar tests (two described in Table 3) reproduced these same phenomena. These small scale tests closely resembled volcanic eruptions (Fig. 3). One of these utilized water-saturated sand and demonstrated the potential of these mildly energetic interactions of the thermite with restricted access to water while producing a slag of agglomerated thermite fragments and sand resembling peperite.

2. Type II—Excess Water, No Confinement. By immersing a fairly large Plexiglas tube of thermite in a box of water, we were able to photograph the interaction of thermite with water. One-hundred kg of thermite were used with about 900 kg of water. The access of water to the thermite was variable during the course of the experiments. In the first experiment initial activity was Strombolian with brief (<1 s) Surtseyan blasts caused by water which apparently had access to the thermite (Fig. 4a). Most of the steam produced was optically transparent (superheated), and the thermite ejecta was not completely quenched (incandescent). The experiment culminated with a Surtseyan blast that destroyed the water box (Fig. 4b). This event was caused by rupture of the Plexiglas tube holding the thermite, which allowed a large amount of melt to mix with the water in a process termed *self-sustained* or *autocatalytic* mixing[18]. The second test with the water box design produced about 50 s of activity similar to the first, and culminated gradually with weak ejections of quenched (black) thermite fragments in an envelope of saturated steam. After most of the thermite had been ejected, there was enough water left in the box to quickly quench the remaining thermite into lumps that spilled down into the water, resembling pillow lava formation.

3. Type III—Confinement Experiments. Adding a burst diaphragm to the top of the vessel resulted in interaction that was indeed impressive, and showed that strong Surtseyan blasts could be simulated. The degree of explosivity was evident for one experiment where a metal plate welded to the bottom of the vessel blew off, and the vessel was launched upward through the ejecta cloud that was already present. Our analysis of the motion picture records indicates that the vessel rose about 180 m which, considering the weight of the vessel, required about 5 MJ of mechanical energy. The vessel contained approximately 70 kg of thermite (~260 MJ thermal energy), indicating ~2 % conversion efficiency (or ratio) of thermal to mechanical energy. Although this value might seem insignificant, the explosive phenomenon certainly was not. This result prompted further experiments to find the maximum efficiency for these water/thermite experiments. The rationale for further experiments was based upon an idealized ther-

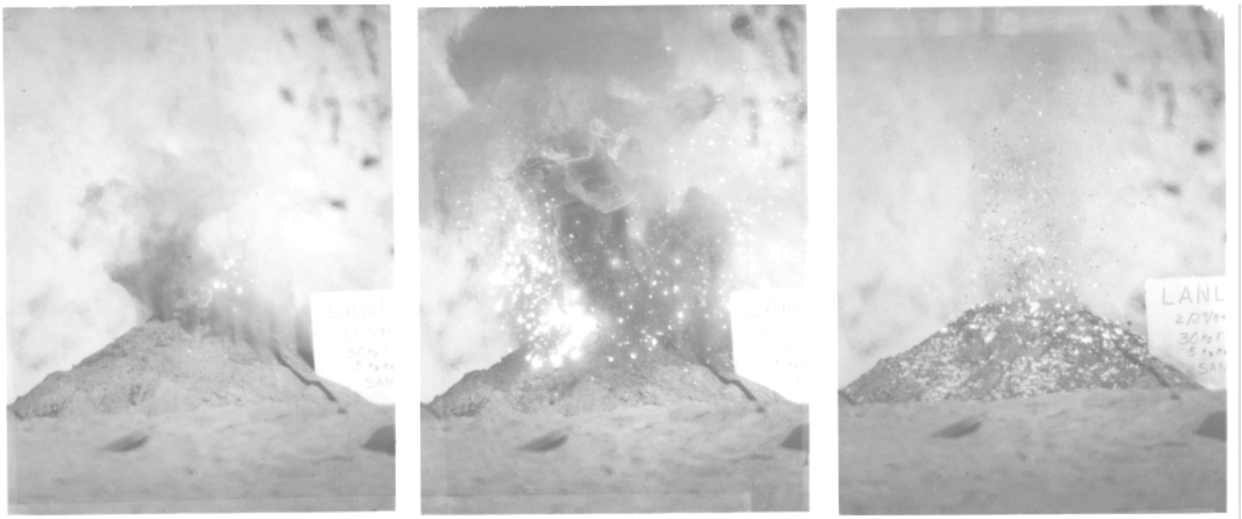

Fig. 3. A series of three photographs depicting the eruption produced by a Type I experimental design (see Fig. 2). The volcano edifice was constructed of sand and is about 0.5 m in diameter and 0.2 m high. Note the cm-size incandescent melt fragments following ballistic trajectories, the black finer grained melt quenched and carried up from the vent in convecting plumes while some moves downslope in a density current, and a small lava flow rivulet running downslope on the right.

Fig. 4. Photographs showing eruption of a Type II experimental design (see Fig. 2). **(a)** Strombolian activity consists of cm-sized, incandescent fragments of melt ejected in ballistic trajectories. The bright area of concentrated ejecta is about 2 m in width. **(b)** Surtseyan activity produced mm- and μm-sized particles blasting upwards and out with complete destruction of the experimental apparatus. The top of the jet reaches about 6 m above the base.

modynamic theory predicting efficiencies as high as ~30% depending upon the water/melt mass ratio and confining pressure[3].

4. Type IV—Confinement Experiments with a Vent Pipe. A vent pipe was incorporated so that the thermite was forced through the water compartment of the vessel during interaction and ejection (Fig. 5). This design was tested (77-1, 77-2, 78-1, 78-2) with the addition of two pressure gauges in the water compartment in order to measure pressure histories. Using various amounts of water, 90 kg of thermite, and burst diaphragms set at 8 MPa for all but one where no diaphragm was used, these experiments showed that all of the thermite was completely ejected from the vessel, indicating good mixing with the water. Pressure records[3] demonstrated the pulsating nature

Fig. 5. Photograph of the Type IV experimental design (see Fig. 2), which consists of a containment vessel (0.6 m x 0.4 m) filled with 90 kg of thermite. This picture with a film box for scale shows the vessel with its top lid removed, exposing the central vent tube through which ejection occurs.

Fig. 6. Photograph showing a Surtseyan jet from Type IV design. The incandescent jet reaches about 15 m high with a dark smoke plume extending above it. The flaring shape of the jet indicates that it is overpressured.

of the interactions and their capability to produce overpressures in excess of 45 MPa, which is above the critical pressure of water. Although all of these experiments produced jets of incandescent ejecta and superheated steam reaching as high as 50 m (Fig. 6), there was considerable variation in pressure histories and development of the ejecta jets between what resembled Strombolian and Surtseyan behavior. Experiment 78-2 employed no burst diaphragm but still produced a Surtseyan burst lasting about 2 s. Experiment 80-7 was used by Wohletz and Sheridan[19] to study some aspects of Martian rampart crater development. The "eruption" lasted about 1 s and produced a jet 40 m high with ejecta velocities approaching 80 m/s as documented by motion pictures. The blast produced a well developed base surge that spread horizontally 6 m outward with a peak velocity of about 15 m/s. The surge pushed over small (25x25 cm) aluminum plates fixed to the ground to a distance of 5 m from the crater. The nearest plate fell toward the crater indicating inward flow at about 1 m from the crater. The crater had a rim diameter of 2.1 m, a rim crest height of 0.27 m above the ground and a depth of 0.33 m. The overall morphology of the crater was that of a tuff ring with 12° outer slopes. Rays of wet, fine-grained ejecta extended through the deposit outward from the crater and contained accretionary lapilli of thermite sticking to surfaces of sand grains.

B. Analysis of Experimental Types I Through IV

By comparing the ejection activity from each of the four designs, measures of confinement strength and rigidity were determined. In experiments using a steel cylinder, the ejecta was directed vertically, whereas the open, more flexible apparatus (water box) provided little constraint on the ejecta. The confinement strength provided by the burst valve, allowed internal pressures to build up until the confining pressure was exceeded. As expected, it was found to increase the explosivity of the experimental eruption.

Grain-size analyses of ejecta recovered from the steel cylinder-central vent experiments were coupled to the recorded pressure-time histories. The pattern of recorded pressurization events were found to resemble the eruption pattern typical of Strombolian and Surtseyan activity[3]. Strombolian-like activity produced centimeter-size fragmental debris and was characterized by pressure oscillations ranging up to 14.0 MPa. These pressure oscillations were harmonic with an average range of frequencies up to

Table 3. Results of Experimental Design Types I through IV.

Experiment	R_m	*Confine-ment*	*Description*
Type I.			
1.	0.19	0.5 m sand	1 to 2 mm diameter melt fragments ejected in a fountain 2 to 3 m high for 4 to 5 s; Hawaiian to weak Strombolian.
2.	0.13	0.5 m sand	1 cm diameter melt fragments ejected in a fountain 7 to 10 m high for 2.5 s using a restricted vent nozzle; strong Strombolian.
3.	0.25	0.2 m sand	Strombolian burst of cm-size melt fragments ballistically ejected 5 m high for <1 s; Surtseyan burst of <1 mm ejecta to 10 m high for <1 s; torus cloud formed.
4.	0.20	0.2 m sand	Strombolian activity for several seconds ballistically ejected cm-size fragments of melt 2 to 5 m into the air; used water saturated sand.
Type II.			
1.	0.1-10.0	none	Variable access of H_2O to melt; Strombolian activity for several minutes with brief Surtseyan blasts lasting <1 s; cm-size fragments ejected ballistically to a height of 10 m; Surtseyan blasts were brilliant hemispherically expanding clouds of μm-size particles enclosed in superheated steam; large Surtseyan blast (<1 s) destroyed water box and produced a horizontally moving surge of incandescent particles and steam.
2.	01.-10.0	none	Variable access of H_2O to melt; 50 s of Strombolian ballistic ejection of cm-size fragments with brief (<1 s) Surtseyan sprays of sub-mm-size quenched particles; 60 s of weak Surtseyan ejection of mm-size quenched melt fragments moved ballistically and in surges with saturated steam; submarine quenching of melt into mm- and cm-size lumps (pillows).
Type III.			
1.	0.45	8.0 MPa	Vessel buried below 1 m of sand; weak Surtseyan ejection of melt in <1 s; eruption column 24 m high with horizontally moving base surge; 1-mm fragments; created a tuff cone 2.5 m in diameter and 0.5 m high at rim; continuous ejecta deposits extended to 5 m from crater rim.
2.	n.d.	8.0 MPa	Weak Surtseyan blast (<1 s); inactive for several s; large explosion tears base of the vessel off and launched the vessel ~180 m into the air.
Type IV.			
77-1	0.31	8.0 MPa	Violent Surtseyan blast for <1 s; eruption column 50 m high; μm-size dust carried away in the wind.
77-2	0.23	8.0 MPa	Surtseyan blast for 16 s; eruption column 35 m high; μm-size particles; superheated steam; strong Strombolian eruption for 90 s included two short (<2 s) Surtseyan blasts; cm-size fragments ejected ballistically; culminating with about 1 minute of weak Hawaiian fountain 10 m high.
78-1	0.26	8.0 MPa	Surtseyan ejection for 5 s of incandescent steam and μm-size particle to 50 m high; pulsating Strombolian and weak Hawaiian bursts each lasting 5 s with melt fountains 10 m high.
78-2	0.22	none	Surtseyan blast for 2 s; μm-size particles and superheated steam jetted 40 m high.
80-7	0.22	8.0 MPa	Vessel buried below 1.3 m of sand using a vent pipe similar that used in Type IV design; strong Surtseyan blast for <1 s; eruption column 40 high; base surge moved 6 m from vent; ejecta consisted of <1-mm-size ejecta and cm-size accretionary lapilli; formed tuff ring 2.1 m in diameter and 0.27 m high at rim; continuous ejecta deposit extended 6 to 7 m from crater rim.

n.d. not documented

15 Hz. Two types of Surtseyan-like activity were recognized, strong and weak, based on pressure-time patterns and grain-size. Strong Surtseyan-like activity produced μm-size fragments and pressure pulses up to 35.0 MPa lasting several seconds. Pressure pulses recorded during weak Surtseyan-like activity were similar in magnitude, lasted for more than 10 s and produced mm-size fragments. The explosivity from each event was measured using the recorded pressure peaks and analyzed with respect to grain-size. The results from this exercise indicate that the average grain-size of the experimental ejecta decreased with increasing explosivity.[3]

The contact geometry and chamber volume were found to affect the number of ejection events such that for larger geometric configurations (*i.e.,* water-box experiments) the number of ejection events increased. An insight on the effect of the water to melt mass ratio (R_m) on the mode of ejection was obtained from the water-box experiments. It was observed that the initial contact between water and thermite involved an R_m of < 0.1, and produced Strombolian-like activity. As the interaction progressed, R_m increased to a value greater than 0.1 changing the ejection mode to Surtseyan-like blasts and surge-like expulsions. The end of the experimental interaction occurred when R_m exceeded 2.0 to 3.0, reducing the activity to passive quenching of the melt.

To quantify the conversion of thermal energy to mechanical energy of ejection for the Type IV experiments, we roughly approximated the ejecta velocity (v_e) by considering the time span of jetting (t), the vent area (A_v) and the ejecta mass and density (m_e and ρ_e, respectively):

$$v_e = m_e / \rho_e A_v t \quad . \qquad (2)$$

Assuming the flow of molten thermite through the vent to be mostly incompressible, the Bernoulli equation

$$p_1 = p_2 + \rho_e\left[\left(v_1^2 - v_2^2\right)/2\right] + \rho_e g\left(z_2 - z_1\right) + \rho_e h_l \qquad (3)$$

allowed us to calculate the driving pressure (p_1) of each experiment, where p_2 is the atmospheric pressure, v_1 and v_2 are the initial and final ejecta velocities, respectively, g is the gravitational acceleration, z_1 and z_2 are the initial and final heights of the ejecta, and h_l is a head loss term approximately constrained for flow in the vent pipe. These pressures were comparable to those measured (3.5 to 46.0 MPa) so that the velocity constraints give measures of the experimental mechanical energies. In addition, adiabatic expansion energies[3] were calculated from the pressure records that closely agreed with calculated mechanical energies. The resulting conversion ratios ranged from about 1.5 to 5.0 %, and showed a positive correlation with water/melt mass ratio (Table 4). Basically, we considered these measurements too crude to pursue. However, they indicated we should implement designs that would allow better control and measurement of the amount of kinetic energy released by the water-melt interaction, which is the main topic of the second part of this paper.

III. LIFTOFF EXPERIMENTS

In order to quantify the water-melt mass ratio and confining pressure controls on the mechanical energy of the interaction, we have developed a fifth design, which was described for the *Series II* experiments of Wohletz and McQueen[3]. In this design a burst valve was placed in the base of the vessel and the ejection of high pressure steam and fragmented thermite passing through the vent caused the vessel to behave like a propulsion rocket [after 1984 informally referred to as the liftoff (LOF) design]. With this design, measurements of the internal pressure history and ejecta characteristics were recorded as was the maximum height reached by the vessel during its launch. The vessel design was also very rugged so that it could be reused numerous times with minimal repair.

The LOF vessel was a thick-walled (6.9 cm) steel cylinder 64.5 cm long and 24.5 cm in outside diameter (Fig. 7). This vessel with about 3 kg of thermite and between 1 and 5 kg water weighed about 250 kg so that the venting would lift it only a few meters. The burst diaphragm was similar to previous designs except that the venting orifice was only 2.5 cm in diameter. A 1.5-mm-thick sheet of polyethylene was used to line the inside of the vessel, which made it considerably easier to clean and refurbish the vessel. Unreacted fine-grained thermite mixture was held above the water by two aluminum plates separated by a 1.6-cm-thick layer of quartzo-feldspathic sand. The Al barrier was melted by the reacting thermite, which allowed the melt to flow downward into the water reservoir.

A useful number for characterizing these experiments is the mass ratio of water to thermite available, R_m. Here the range of R_m values investigated was limited by the volume of the vessel's inner chamber. Excluding the thickness of both sand and partition, the total depth of water and melt had to be less than 59.0 cm restricting the relative amounts of melt and water used. For most experiments, between 2 and 4 kg of thermite were used with varying proportions of water. The minimum R_m was 0.38 and used 1.82 kg of water and 4.73 kg of melt. The maximum R_m was 2.00 and used 4.00 kg of water and 2.00 kg of melt.

The burst diaphragms were made of aluminum disks with orthogonal crossing grooves machined in the bottom face. The diaphragms provided varying confinement pressures (p_{conf}), depending on the depth of the grooves. These were calibrated by pressurizing the water-filled vessel with air. Three confining pressures were used; (1) 6.8 MPa; (2) 16.3 MPa; and (3) 35.7 MPa; the last exceeds the critical pressure of water (22.0 MPa).

Forty experiments were completed of which 33 gave usable records. Seven of the experiments failed to lift off due to either failure of vessel seals, malfunction of the ignitor, or premature failure of the burst valve. Five other experiments did not lift off because of insufficient internal pressurization. Table 5 lists values of R_m, mass of water,

Table 4. Preliminary Conversion Ratio Calculations*.

Experiment	*Water/Melt Mass Ratio* (R_m)	*Jet Height* (m)	*Ejecta Velocity* (m/s)	*Measured Pressure* (MPa)	*Calculated Pressure* (MPa)	*Mechanical Conversion Ratio* (%)	*Adiabatic Conversion Ratio* (%)
77-1	0.31	50	90	46.0	42.3	4.90	4.48
77-2	0.23	35	40	18.2	18.1	2.83	3.26
78-1	0.26	50	60	20.9	24.2	3.62	3.89
78-2	0.22	40	30	3.5	10.2	1.68	3.56

* Conversion ratios are the ratio, to the initial thermal energy of the thermite melt, of the mechanical energy ($m_e v_e^2/2 + m_e g z_2 + h_l$) and adiabatic expansion work (change in steam internal energy upon expansion to atmospheric pressure from known initial pressure and volume in the experimental vessel).

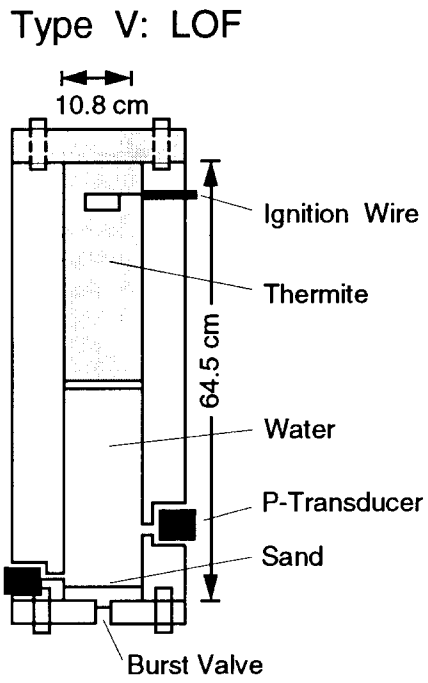

Fig. 7. Schematic illustration of the Type V (LOF) experimental vessel design. Nearly 7-cm-thick iron walls were used to ensure vessel stability from rupture. Thermite was ignited in the upper partition of the vessel and allowed to melt through an aluminum partition to contact water below. When pressure rose to values in excess of the burst valve strength, venting occurred from the vessel's base producing a jet of steam and thermite fragments that propelled the nearly 250-kg vessel into the air.

mass of melt, and p_{conf} for the 33 experiments analyzed in detail.

The vessel was instrumented with up to four quartz pressure transducers mounted in the water reservoir of the vessel (Fig. 7 and Fig. 8). The pressure gauges were used to record the pressurization produced by the melt-water interaction in the lower chamber from the time of ignition until the burst valve opened. The gauges were triggered either manually at the time of ignition or by internal signal-driven triggers activated by a pressure rise.

The acceleration and flight-path of the vessel were recorded using a pair of potentiometers that were coupled so that the voltage was proportional to the motion of the vessel. These gauges, mounted on a launch gantry (Fig. 8), were triggered by shorting of coaxial pins placed on the burst valve. Output readings were recorded on strip charts and oscilloscopes. 16 mm and 35 mm motion picture cameras running at about 144 and 48 frames per second respectively were used to record the events. These records provide information on ejecta velocities, their size and shape, the height and acceleration of the vessel and, to some degree, the temperatures involved.

We need to quantify the proportion of the initial melt internal energy converted into the mechanical energy imparted to the vessel and ejecta for each experiment. For this exercise the total kinetic energy of the vessel and ejecta are calculated from the camera and potentiometer records, while steam expansion energy is calculated from pressure records, assuming both adiabatic and isothermal expansions after initial thermal equilibrium between the melt and water. By dividing the calculated kinetic, adiabatic, and isothermal energies by the initial melt internal energy, three conversion ratios are defined. Because the calculated expansion energies are greater than the observed kinetic energies, the discrepancy between the two is considered to be a rough estimate of the degree to which the melt and water reached thermal equilibrium prior to burst.

Further analysis concerns the correlation of the pressure-time records with conversion ratios and ejecta clast morphologies, determined by scanning electron microscopy (SEM) for each experiment. Several distinct pressure record types are found to correlate with the magnitudes of calculated conversion ratios and observed clast morphologies, which allow some speculation regarding the nature of melt fragmentation and mixing with water.

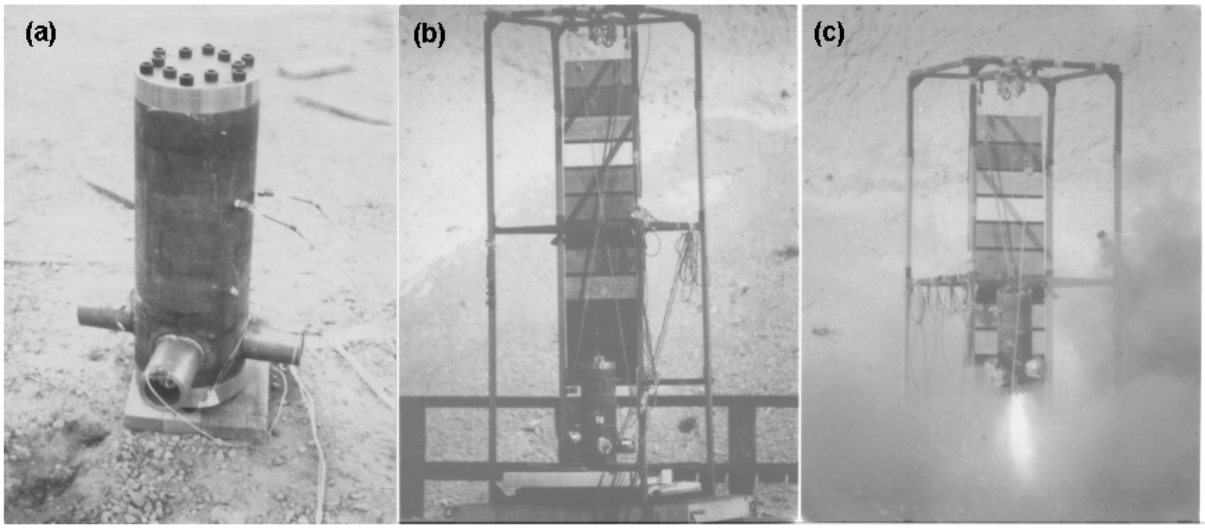

Fig. 8 **(a)** Photograph of the Type V (LOF) vessel (0.7 m high), showing cylindrical pressure gauge ports at its base with gauge and ignitor leads attached. **(b)** Photograph of the launching gantry used for the LOF experiments. The gantry supported velocity potentiometers at its top and is painted for background. **(c)** Photograph showing the LOF vessel rising off the firing table. The fiery jet extends about 1 m downward from the vessel's base.

Because chemical alteration is a common characteristic of hydrovolcanic ejecta, attempts were made to study some chemical kinetics involved in the water and melt interaction. For this work, we focused on oxygen isotope exchange between the water and the thermite melt. Like magma, thermite is relatively rich in heavy oxygen ($\delta^{18}O$ ≈ 10 to 16 ‰) while the tap water used in the experiments has an oxygen composition typical of groundwater ($\delta^{18}O$ ≈ -12 ‰). By comparing the isotopic compositions of the starting thermite and water to that of ejecta formed by the interaction, we tested the hypothesis that exchange of the oxygen isotopes during interaction should be small, far from obtaining equilibrium values. This hypothesis is based on the premise that oxygen diffusion rates are sufficiently small that little exchange could occur within the duration of the experiments.

IV. EXPERIMENTAL RESULTS

In general, a successful experiment was one in which the chamber pressurized, in less than 20.0 s after ignition, to a magnitude that opened the burst valve and ejected a highly pressurized mixture of water-vapor-fragmental ejecta in the form of a jet. The impulsive force of the jet propelled the vessel into the air, and a maximum height was attained in less than one second. Twenty-eight experiments resulted in measurable liftoff, reaching liftoff heights (LOH) between 0.02 and 3.55 m (Table 5); of these, 21 provided usable pressure records for which maximum pressures (p_{burst}) could be evaluated. Frame-to-frame analysis of film records revealed that a gray cloud of steam and ash formed upon liftoff. The majority of fragmental debris was ejected prior to landing and was typically incandescent.

A. Trajectory Records

The trajectory path of the vessel was predominantly vertical during ascent with some tipping near landing (Fig. 8). For the successful experiments, the vertical flight path was recorded as a function of time on strip charts and/or oscilloscopes coupled to potentiometers that followed the vessel motion. These records were verified by the photographic records; the maximum heights agreed well. Recorded maximum liftoff heights are listed in Table 5. The flight path records (Fig. 9) give estimates on the ascent rate and the time interval of acceleration. Both were required for the analysis and integration of pressure histories.

B. Pressure Records

At least one pressure record was obtained from a successful experiment with the exception of nine experiments where either faulty connections or severing of the connections upon liftoff made the records unreliable. For the 15 experiments that had more than one pressure record, the pressure-time traces were transposed and found to match well except for a slight offset in magnitude, which was most likely a function of transducer location. The recorded burst pressure (p_{burst}; Table 5) did not in many cases match the pressure provided by the burst valve (p_{conf}). Inspection of the burst valve indicated that in some experiments the

valve failed by melting and allowed burst to occur at a lower pressure. In some cases it was possible that the

Table 5. LOF Experimental Conditions and Results

Experiment	R_m	*Water (kg)*	*Thermite (kg)*	p_{conf} *(MPa)*	*LOH (m)*	p_{burst} *(MPa)*
80-1	0.96	2.55	2.65	6.1	0.90	3.60
80-3	0.49	2.25	4.57	6.8	1.50	9.80
80-4	0.62	2.78	4.50	16.3	0.96	0.85
80-5	0.66	2.78	4.20	15.0	1.33	8.40
80-6	0.66	2.78	4.20	35.7	0.0	n.d.
81-1	0.38	1.82	4.73	16.3	2.00	33.00
81-2	1.20	3.53	2.94	16.3	1.39	n.d.
82-1	1.06	3.21	3.02	16.3	1.44	10.00
82-4	1.00	3.00	3.00	16.3	0.36	2.40
82-5	1.00	3.00	3.00	16.3	0.35	n.d.
82-6	1.00	3.00	3.00	35.7	2.40	n.d.
82-7	1.00	3.00	3.00	16.3	0.60	n.d.
82-9	0.67	0.20	3.00	16.3	1.51	n.d.
LOF-1	1.00	3.00	3.00	6.8	1.08	23.00
LOF-2	1.50	3.00	2.00	6.8	0.0	9.70
LOF-5	0.73	3.00	4.10	16.3	2.70	n.d.
LOF-6	0.67	2.00	3.00	16.3	1.36	15.00
LOF-7	1.50	3.00	2.00	16.3	0.41	11.00
LOF-8	1.15	3.00	2.60	35.7	2.70	23.90
LOF-11	1.00	3.00	3.00	16.3	3.55	61.20
LOF-12	1.25	2.50	2.00	16.3	0.12	n.d.
LOF-13	2.00	4.00	2.00	16.3	1.08	18.00
LOF-14	1.60	4.00	2.50	35.7	1.64	41.70
LOF-15	0.67	1.67	2.50	35.7	0.0	8.70
LOF-16	0.67	1.60	2.40	35.7	0.0	n.d.
LOF-17	0.67	1.60	2.40	35.7	0.02	13.60
LOF-18	0.69	2.20	3.20	16.3	0.30	12.00
LOF-19	0.69	2.20	3.20	16.3	1.10	n.d.
LOF-20	0.69	2.20	3.20	16.3	0.12	n.d.
LOF-21	0.69	2.20	3.20	16.3	0.0	n.d.
LOF-22	1.20	3.60	3.00	16.3	1.04	11.61
LOF-23	1.31	3.60	2.74	35.7	2.90	21.30
LOF-24	0.95	3.10	3.26	35.7	2.01	37.00

n.d. - not determined

transducer never recorded the actual burst pressure because its duration was too short to record. In other cases, the burst pressure was much greater than the confining pressure, which suggests that the valve did not respond to the pressure as fast as it was rising.

The pressurization history of the chamber was characterized by a variety of curves, ranging from a single pressure pulse to a series of additive pressure rises. Figure 10 illustrates some typical pressure histories. In seven experiments, recorded burst pressures exceeded the confining pressure (Table 5). These pressure records are classified into three distinct groups, each corresponding to a specific range of LOH: (1) pressure group I (P-I) with LOH > 1.45 m ; (2) P-II with 0.60 m < LOH < 1.45 m; and (3) P-III with LOH < 0.60 m. A representative pressure-time curve is illustrated in Figure 11 for each of these groups. Later analyses of the experiments will retain these groupings.

P-I experiments recorded exponential pressure-time curves reaching pressures from 9.8 MPa to more than 61.2 MPa within a time frame between 0.9 s and 2.3 s (Fig. 11a). All recorded burst pressures exceed the confining pressure by up to a factor of three.

P-II experiments were characterized by an initial linear pressure rise to a pressure between 0.2 MPa and 11.5 MPa, and after approximately 0.3 s and 0.8 s, the pressure increased to a value near the designed pressure (Figs. 11b

and c). Several experimental systems recorded a terminating pressure spike (Fig. 11b). Typical time frames for the P-II pressurization events ranged between 1.3 s and 5.4 s.

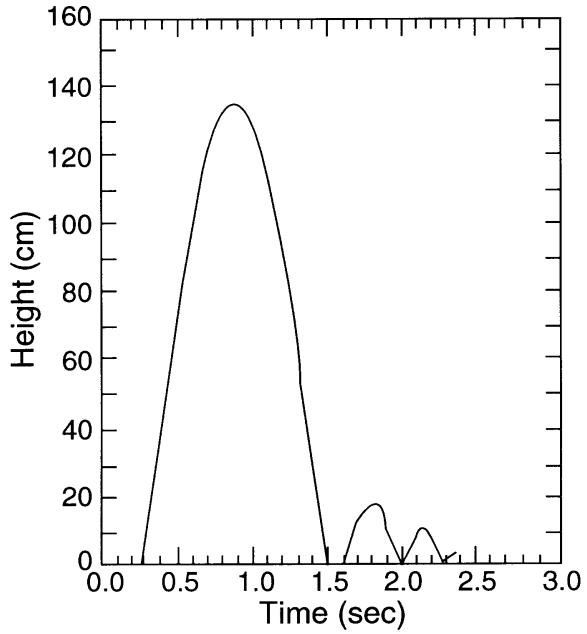

Fig. 9. Example trajectory record from experiment LOF-6. The maximum liftoff height (1.37 m) corresponds to the first peak; subsequent peaks record bouncing of the vessel on the firing table after its flight.

P-III experiments were characterized by an initial linear pressure increase to 2.0 MPa immediately followed by an event that pressurized the chamber to a maximum value within a time span ranging from 5 to 20 s (Fig. 11d). The pressure then remained at this value (2.3 MPa to 13.4 MPa) until the chamber burst. The distinguishing feature of P-III experiments is that the recorded burst pressure is significantly lower than the designed value of the valve by up to 22.1 MPa (*e.g.*, LOF-17). However, six experiments did record liftoff because the burst valve failed by melting (rather than overpressure) caused by melt accumulating in the base of the chamber. Experiments 82-7 and LOF-7 display records that could also be assigned to the P-II group, but their LOH and ejecta characteristics suggest their inclusion in the P-III group.

C. Experimental Ejecta Size and Morphology

Samples of ejected material, including a sample of unreacted thermite for control, were recovered from 10 experiments. These samples may not completely represent the total grain size distribution of clasts produced from each experiment due to the fact that the finest material was commonly observed to be carried away in a steam cloud. Experimental ejecta clast sizes and morphologies were studied utilizing automated digital scanning electron microscopy (SEM) for the purpose of quantifying clast shapes and size distributions.

Six experimental samples were chosen for detailed study. Each sample was sieved and clasts from the coarse and fine modes were analyzed; the fine mode was less than 63 μm, and the coarse mode ranged between 125 μm and 1000 μm. Although our sampling did not adequately represent the fraction of the sample finer than 62 μm (4 ϕ), the distributions shown in Figure 12 are very similar to many hydrovolcanic tephra size distributions[20]. Each sample distribution is shown in Figure 12 to be composed of several subpopulations (dashed numbered curves). These subpopulations are found through application of sequential fragmentation/transport theory[20] (SFT), and they represent fractions of each sample having distinct density and shape characteristics and fragmentation origins. For example, the narrow peaked subpopulations show distribution characteristics produced by hydrodynamic instabilities, whereas the broader subpopulations are characteristic of fragmentation caused by brittle failure.

Digitized screen images of several hundred particles in each sample provided data for numerical representations of size and shape. In Table 6, clast shapes are described by a shape factor (S_f) defined as $S_f = P^2 / (4 \pi A_r)$, where P and A_r are the perimeter and the cross sectional area of a clast.[20] $S_f \cong 1$ for spherical and blocky equant particles, and it increases as particle shapes become elongated, convoluted, and aggregated (agglomerated) with large surface area.

The results from the shape factor and qualitative morphologic analysis identified six distinct clast types that are described as follows:

Type 1: Blocky, equant to tabular in shape having smooth, planar to curviplanar surfaces. Clasts of this type are most abundant in the coarse fraction (>125.0 μm) and correspond to S_f between 1.3 to 5.3.

Type 2: Irregular shapes with smooth, fluid-like surfaces and quenched textures. Clasts of this type are most abundant in the coarse fraction (> 63.0 μm) and have respective S_f values between 2.0 to 3.5.

Type 3: Moss-like, convoluted shapes with highly irregular surfaces formed by annealed fine-grained particles. Clasts of this type are most abundant in the coarse fraction (>125.0 μm) and have respective S_f values greater than 12.0, although S_f values for samples LOF-11

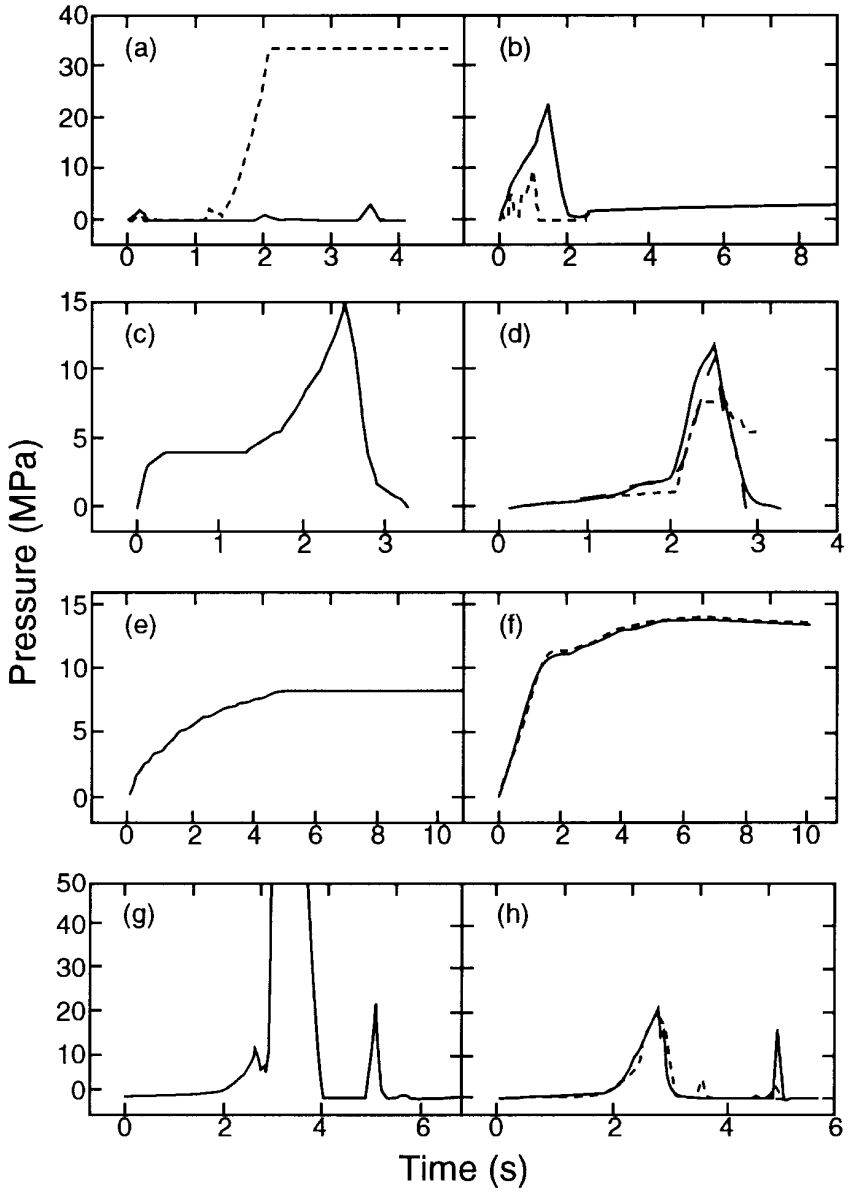

Fig. 10. Examples of pressure records; lines of different styles show traces obtained from different transducers on the same experiment. **(a)** Two pressure perturbations preceding an exponential pressure rise were recorded during experiment 81-1. The recording range of the pressure transducer was exceeded during this experiment, hence a minimum of 33.0 MPa is assumed for the burst pressure. **(b)** Two pressure-time traces were recovered from experiment LOF-1. One recorded a series of additive pressure pulses that reached a maximum pressure of 9.8 MPa within 1.3 s. The other recorded an initial parabolic rise up to a pressure of 14.8 MPa within 0.94 s followed by a linear increase to 22.6 MPa. Although there was a discrepancy in the magnitude of the recorded burst pressure, the pressurization time interval was the same on both transducer recordings. A magnitude of 22.6 MPa is assumed for the chamber pressure at burst. **(c)** In experiment LOF-6 a burst pressure of 15.0 MPa was reached after 2.54 s. An initial parabolic event pressurized the chamber to about 3.9 MPa, which was followed 0.9 s later by an event that pressurized the chamber to the recorded burst value. **(d)** All three pressure-time traces were recovered from experiment LOF-7; each recorded the onset of the pressurization event; however, only two recorded the complete event. The initial event reached a pressure of 1.7 MPa within 1.6 s and, after 0.3s, pressurized the chamber to 11.7 MPa within 0.6 s. **(e)** A single continuous parabolic event was recorded during experiment LOF-15, reaching a maximum pressure of 8.0 MPa in 4.5 s. The chamber pressure remained at this value for at least 10.0 s. The time interval to burst was not recorded for this experiment and a minimum burst pressure of 8.0 MPa is assumed. **(f)** In experiment LOF-17 the two pressure-time traces recovered recorded the same event. A maximum pressure of 14.0 MPa was attained by about 6.0 s. As in experiment LOF-15, the time interval to burst was not recorded and a minimum burst pressure of 14.0 MPa was assumed for this experiment. **(g)** For experiment LOF-22 the observed burst pressure was 11.6 MPa which was attained approximately 9.0 s after ignition. The pressure-time trace shows that the burst pressure was reached by a exponential rise within 2.65 s. Immediately after burst, a pressure spike was recorded, which was thought to be caused by vaporization of water upon decompression. **(h)** Three pressure-time traces were recovered from experiment LOF-23, all of which recorded a burst pressure of 21.3 MPa. The recorded burst pressure was attained within 2.8 s by an exponential pressurization event.

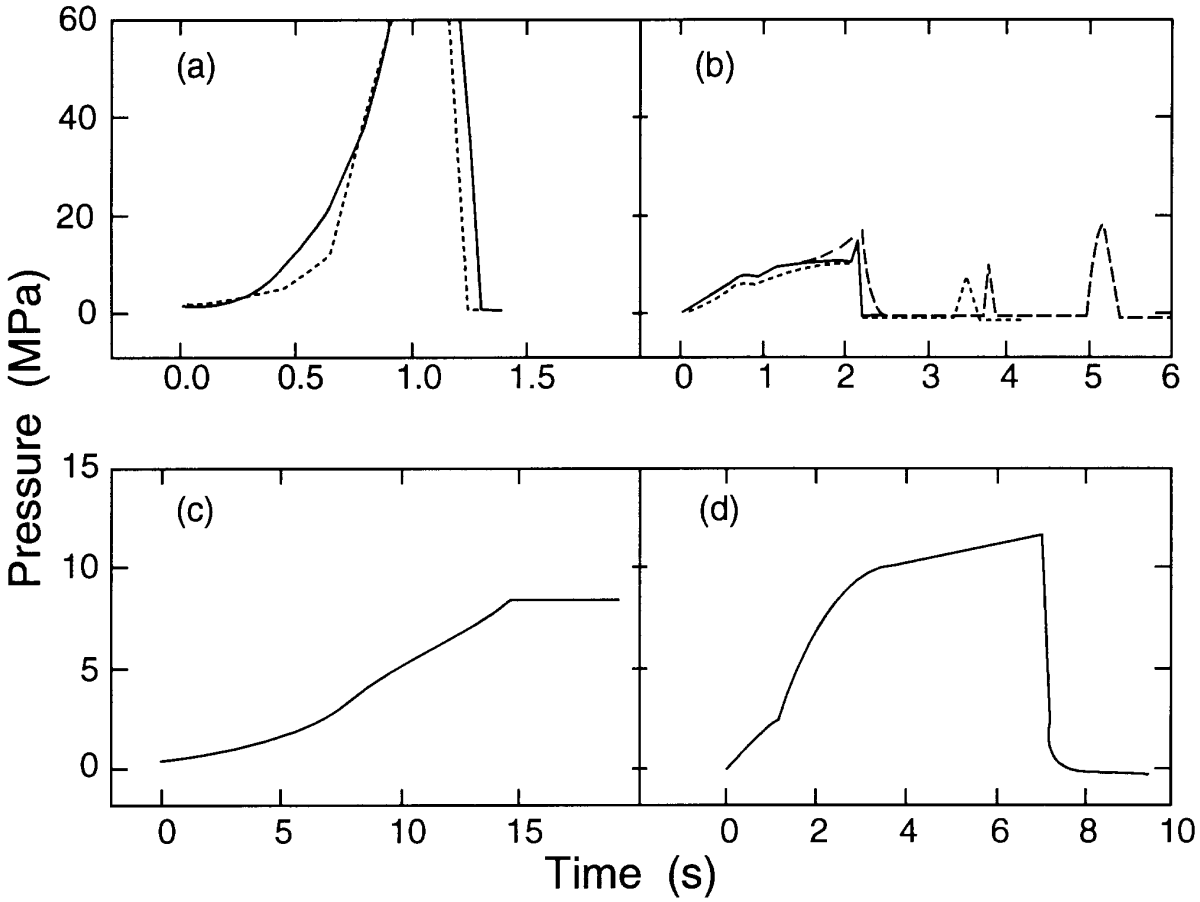

Fig. 11. Example pressure records illustrating the three generalized pressurization histories (different line styles designate the records from different transducers). **(a)** P-I experiments show a sharp exponential pressure rise in less than 1 s in many cases exceeding the designed burst strength of the vessel. In experiment LOF-11, the two pressure-time traces recovered recorded a continuous exponential pressure rise to at least 61.2 MPa in less than 0.9s. A minimum burst pressure of 61.2 MPa is assumed for this experiment, as the recording rate of the pressure transducers was inadequate to record the entire event. **(b)** P-II experiments show a generally linear rise of pressure with time. Four pressure-time traces were recovered from experiment LOF-13. All recorded the same sequence of events up to the burst time. The initial pressurization event was roughly linear reaching a pressure of 7.1 MPa within 0.8 s. After 0.1s at a pressure of 7.1 MPa, a parabolic rise occurred which raised the chamber pressure to 13.8 MPa within 1.3 s. Preceding the second event was a pressure spike, which raised the chamber pressure instantaneously to 18.2 MPa. The two pressure pulses that occurred after burst resulted from the impact of the vessel upon landing. **(c)** In experiment 80-5, two linear events pressurized the chamber to at least 8.4 MPa within 14.7 s; the horizontal line at 8.4 MPa suggest that the strip chart recorder malfunctioned before burst occurred. **(d)** P-III experiments (LOF-18) have a parabolic rise in pressure.

and 82-6 show lower averages, being similar to those other relatively equant clasts.

Type 4: Spherical to drop-like in shape. Surfaces are rough to smooth and spheres are found to be either hollow or solid. These clasts are most abundant in the fine fraction (<88.0 μm) and have S_f values of 1.0 to 1.3.

Type 5: Plate-like to crescent-like in shape. Surfaces are commonly smooth and edges are slightly round due to reheating. These clasts are most abundant in the fine fraction (<88.0 mm) and have S_f values between 2.9 to 3.3.

Type 6: Aggregates formed by numerous partially annealed clasts of Types 1, 4, and 5. These appear as small clasts fused to the surface of a large single clast or as fused clasts uniform in size. This clast type is most abundant in the coarse fraction (>360.0 μm) and has an S_f range generally greater than 5.0.

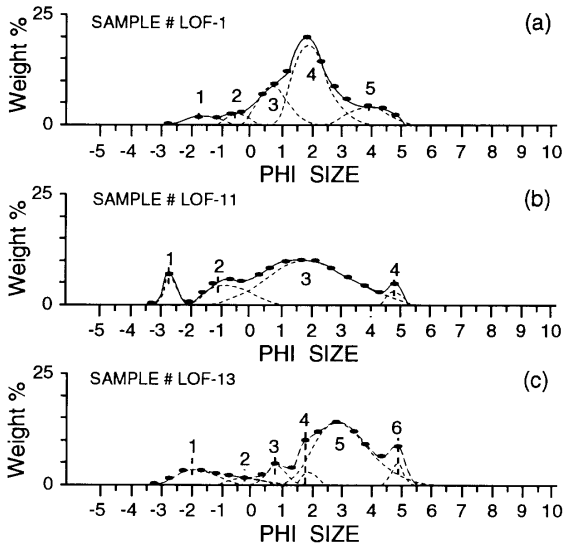

Fig. 12. Results of sieve analysis of three samples of experimental debris. Sample characterization where ϕ = - $\log_2$ (diameter in mm) includes: **(a)** LOF-1 with mean ϕ = 1.74 and standard deviation (σ) = 1.45; **(b)** LOF-11 with mean ϕ = 1.25 and σ = 1.99; and **(c)** LOF-13 with mean ϕ = 2.19 and σ = 1.90.

These clast types show a strong resemblance to the five type clasts identified by Wohletz[21] as diagnostic products of hydrovolcanic events. The sixth clast type is an aggregate clast and will be described in detail later.

Each sample is characterized by several of the six clast types listed in Table 6 along with the mean shape factor and the standard deviation for the respective experiment. Samples recovered from experiments LOF-11 and 82-6 contain predominantly Type 3 clasts in both size fractions. Type 3 clasts are characterized by fine-grained nodular surfaces (Fig 13). Elongate Type 1 clasts are a minor component in the LOF-11 sample and have curviplanar surfaces (Fig. 13a). The mossy Type 3 clasts produced from experiment 82-6 are bulbous in shape and have very fine-grained nodule surfaces (Fig. 13c). In the coarse fraction, the mossy clasts have at least one smooth, planar fracture surface commonly containing clusters of cavities (Fig. 13d). The cavities are cylindrical and relatively deep.

Sample 82-1 is comprised of Types 6 and 5 with Type 4 as a minor component (Fig. 14a). Type 6 are formed by fine-grained spherical to drop-like particles annealed to surfaces of larger core clasts (Fig. 14b). The basal surfaces of the core clasts appear wavy in texture. Type 5 clasts are typically elongated, cuspidate shapes. Individual spherical shapes typify Type 4 clasts in this sample; rarely are botryoidal masses observed.

Types 6 and 1 are the dominant shapes in sample LOF-1; Type 4 is subordinate in the fine fraction (Fig. 14c). Type 6 are formed by very fine-grained spherical to blocky particles annealed to the surface of larger core clasts. The basal surfaces of the core clasts appear hummocky in texture as shown in Figure 14d. Type 1 clasts are elongate to equant in shape with smooth planar surfaces. Type 4 are characterized by spherical and dumbbell shapes, and grape-like masses.

The fine-fraction from sample LOF-13 is comprised of Types 5 and 2, with Type 4 clasts being a minor component (Fig. 14e). Type 5 are plate-like to crescent-like in shape. Spherical to drop-like shapes characterized Type 4 clasts. Type 2 clasts in this sample have smooth, hummocky surfaces with few or no adhering particles and appear slightly vesicular (Fig. 14e). Type 6 clasts are most abundant in the coarse fraction and are typically comprised of fused hollow spheres, and blocky and tabular clasts of uniform size (Fig. 14f).

Sample 82-7 contains mostly Type 1 in the fine mode with Type 4 being a minor component, and Type 2 in the coarse mode (Fig. 15a). Type 1 clasts are commonly tabular and polygonal in shape. Type 4 are spherical to dumbbell in shape and make up the very finest particles in the sample. Type 2 clasts appear as irregular shaped masses with poorly vesicular, hummocky, fluidal surfaces with quenched textural features (Figs. 15b and 15c).

D. Oxygen Isotopes

Taylor and Wohletz[22] calculated closed system equilibrium ($\delta^{18}O_{thermite}$ - $\delta^{18}O_{water}$) values at 200 to 500°C to be -6.3 to -8.3‰ for these experiments. We observed up to 30% exchange of ^{18}O, corresponding to 20% of equilibrium values. Figure 16 shows the shift in thermite oxygen composition as a function of R_m. These results indicate that greater water availability and enhanced interaction leads to dynamic chemical kinetics where high temperature, pressure, and reaction surface area promote rapid migration of chemical species. Smith[23] found that fresh, pumiceous samples of postcollapse rhyolite of the Long Valley caldera, California showed $\delta^{18}O$ ⊕ 0 ‰ in contrast to 6.7 to 7.4 ‰ values for obsidian, which are typical values of most unaltered volcanic rocks. His results indicate about a 33% exchange of oxygen between meteoric water and the rhyolite during the formation of the pumice.

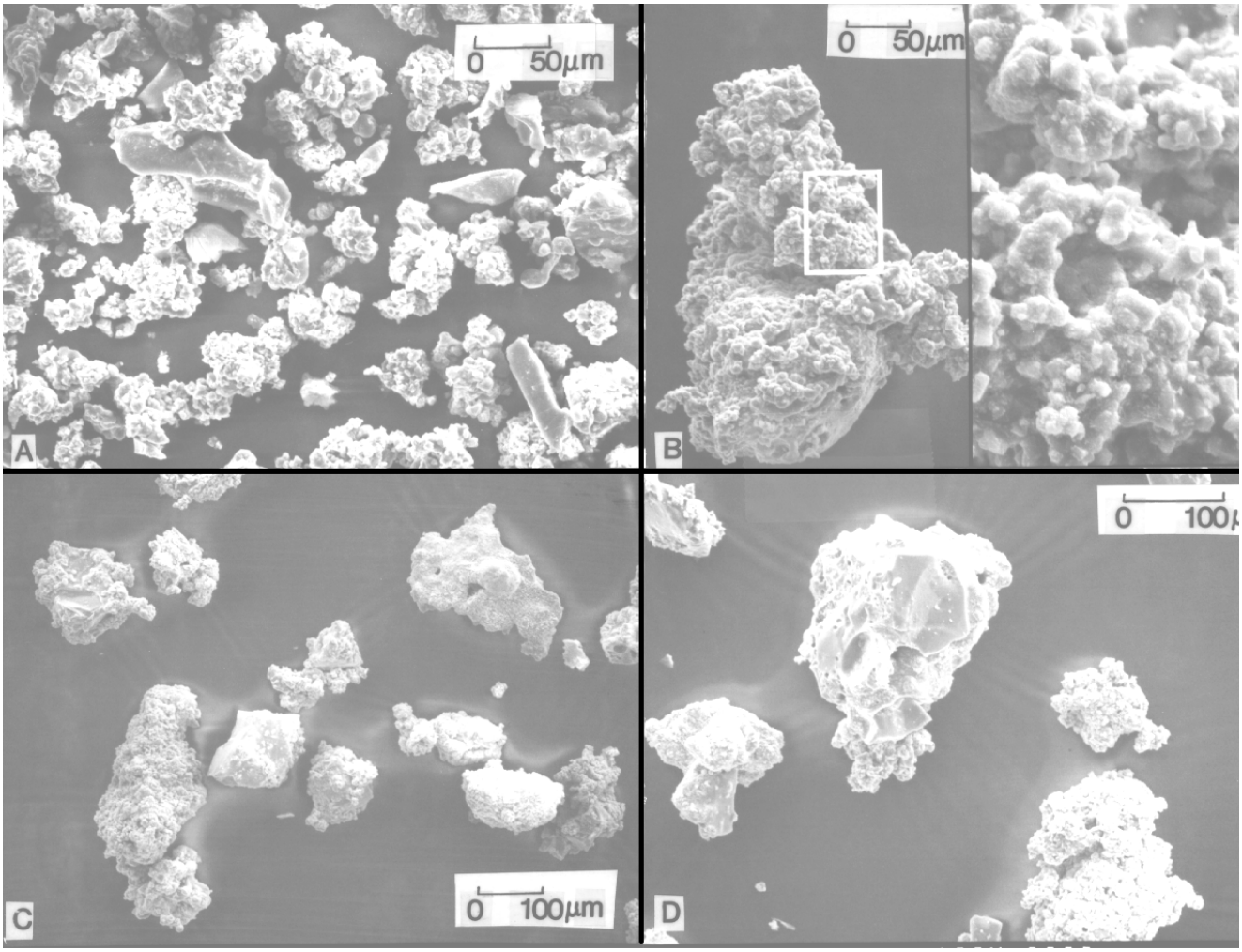

Fig. 13. SEMs of experimental ejecta clasts. **(a)** Moss-like, high surface area particles (Type 3) and a few blocky ones (Type 1) from LOF-11. **(b)** Coarse fraction Type 3 clasts from LOF-11. **(c)** Fine fraction Type 3 clasts from 82-6. **(d)** Coarse fraction Type 3 clasts from 82-6.

V. ANALYSIS

One of the goals of this study was to learn how the water-to-melt ratio and confining pressure controlled explosive energy as manifested by the vessel's pressurization, liftoff, and ejecta characteristics. The explosive energy of the experiments was manifested by the change in the vessel's potential energy (LOH) during its propulsion, the kinetic energy of the ejecta, and burst pressures (p_{burst}). These energies are analogous to those of a volcano where explosive energy is dominantly partitioned into acceleration of tephra and expanding gases in the eruption column as well as excavation of the vent to form a crater.

In order to facilitate the use of these experiments as analogs of hydrovolcanic eruptions of much larger scale, we express the explosive energy as the ratio of the measured and calculated mechanical energy to the initial internal (thermal) energy of the melt. This ratio is called the conversion ratio (CR). Three methods were used to calculate CR for these experiments. The first method is based upon observed values of mechanical energy (kinetic energy of the ejecta, change in potential energy of the vessel throughout its time of flight, and energy expended by movement of air due to drag on the ejecta). This method (MCR) relies on the conservation of momentum. The other two methods are based on thermodynamic calculations. For the thermodynamic calculations we assume initial thermal equilibrium between melt and water by energy balance[24], a function of R_m, and the water density is constrained by its mass and the volume to which it can expand in the vessel prior to burst. For the reversible *adiabatic* (isentropic) expansion model (ACR), the high temperature

and pressure water is assumed to expand along an isentrope after the

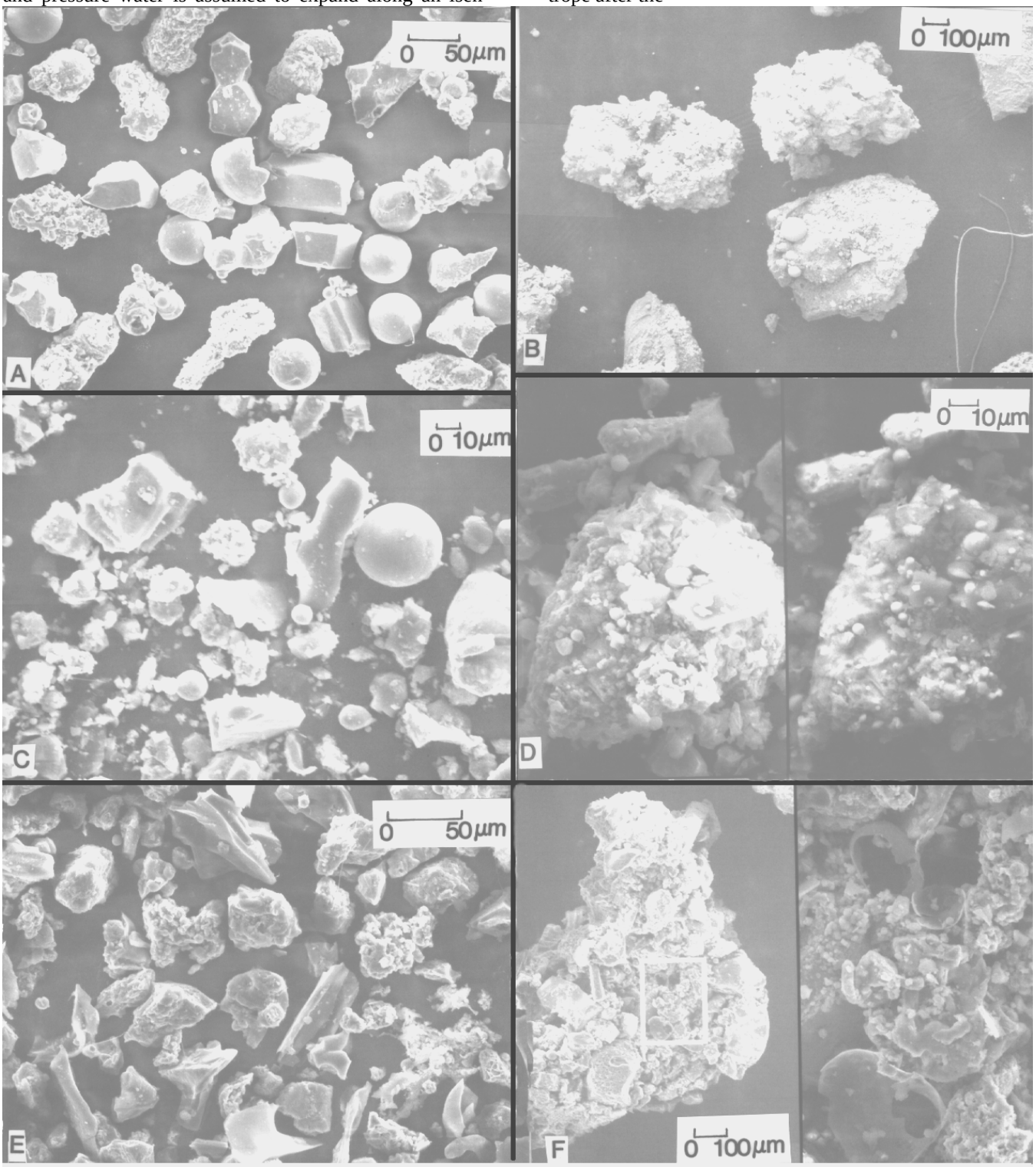

Fig. 14. SEMs of experimental ejecta clasts. **(a)** Type 1 and 4 clasts are evident in the fine fraction of 82-1. **(b)** Type 6 clasts in coarse fraction of 82-1. **(c)** Type 1, 4, and 6 in fine fraction of LOF-1. **(d)** Type 6 in coarse fraction of LOF-1. **(e)** Types 5, 6, and 2 in the fine fraction of LOF-13. **(f)** Type 6 in the coarse fraction of LOF-13.

Table 6. Size and Shape Analysis of Experimental Ejecta.

Experiment	*LOH (m)*	*Particles*[a]	*SEM Diameter*[b] *(μm)*	*Sieve Diameter*[c] *(μm)*	*Shape Factor*[d] *(S_f)*	*Clast Types*[e]
LOF-11	3.55	c: 94	333	420	2.01	3, (1)
		f: 180	78		1.47	3, (1)
82-6	2.40	c: 88	599		4.42	3
		f: 292	181		1.43	3
82-1	1.44					
		f: 366	52		1.76	6, 5, (4)
LOF-1	1.08	c: 121	726	395	2.25	6, (4)
		f: 185	141		1.50	6, 1, 4
LOF-13	1.08	c: 105	936	219	1.47	5, 2, (4)
		f: 193	87		1.20	6
82-7	0.60					
		f: 210	76		1.23	1, 2, (5), (4)

[a] The number of particles analyzed for the coarse (c; 125 to 1000 μm) and fine (f; <63 μm) splits, respectively. Shape factors and dominant clast types are listed for each of the splits.
[b] Mean diameters from SEM analysis.
[c] Only 3 samples were considered representative enough to report sieve mean diameters.
[d] Average shape factor for the entire sample.
[e] Dominant clast types as described in the text; subordinate clast types shown in parentheses.

containing vessel bursts. In the *isothermal* model (ICR), water is in continuous thermal equilibrium with the hot thermite fragments during post-burst expansion. The isothermal model only partially approximates true isothermal behavior because the temperature of the thermite ejecta falls as it transmits heat to the water so that the *mixture* of water and hot ejecta expand along an isentrope. The degree to which true isothermal behavior is approached increases with R_m.

A. Mechanical Energy Conversion Ratios

The kinetic energy of each liftoff event was evaluated by an integral formulation of momentum conservation for which the impulse force equals the change in momentum of the ejecta with the forces of gravity and drag acting on the vessel and the ejecta. The impulse force from the ejecta required to launch the vessel to its measured maximum height (LOH) is equal to the time-integral $[A_n \int p(t)dt]$ of the vessel pressure, $p(t)$, which forced the ejecta through the burst-valve nozzle of area A_n. By differentiation of the vessel's trajectory curve (Fig. 9), the duration of acceleration is found. With the integration interval determined, pressure records were graphically integrated to evaluate the impulse force.

Based on the measurements of LOH, ejecta velocities (u_e) were calculated from Equation (9) to range from 220 to 328 m/s, as listed in Table 7. Because u_e is primarily a function of LOH, we plot the variation of LOH with R_m in Figure 17. This figure shows a crude lognormal relationship of LOH with R_m where experiments of different confining pressures are differentiated. This relationship was theoretically established by Wohletz[24], who found that the conversion efficiency of heat to mechanical energy in water/magma interactions should be of the lognormal form $f(R_m) = a \exp\{-b [\ln(R_m)/c]^2\}$, where a, b, and c are constants and $f(R_m)$ is nearly zero at for R_m at 0 and $R_m > 10$. Hence, other manifestations of mechanical energy are also expected to follow this lognormal relationship.

Knowing the ejecta mass (m_e) and its calculated ejection velocity (u_e from Appendix A), we compute the mechanical energy conversion ratio (MCR), defined as the ratio of kinetic energy of ejecta to the internal heat energy of the melt:

$$\mathrm{MCR} = \frac{\frac{1}{2} m_e u_e^2}{m_m C_m \Delta T} \quad , \qquad (4)$$

where m_m is the mass of thermite and $C_m \Delta T$ is the initial specific internal energy (enthalpy) of the molten thermite (Table 2).

The correlation between the mechanical energy conversion ratio and liftoff height has been analyzed in order to evaluate the effects of both confining pressure and R_m on the efficiency of the water/melt interaction (Fig. 18). A positive correlation is found between the two parameters, defined by the best-fit lognormal curve described above.

Many of the experiments have similar LOH values, yet the MCR values differ considerably which will be shown to be

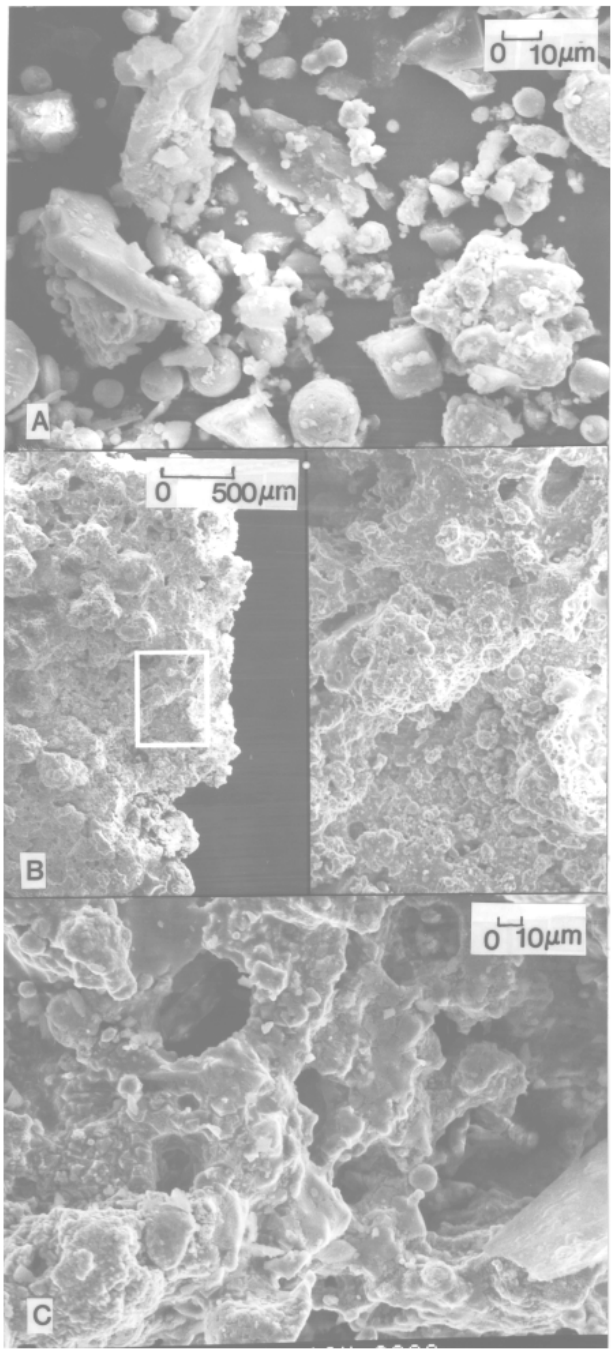

Fig. 15. SEMs of experimental ejecta clasts from 82-7. **(a)** Type 5, 2, and 4 in the fine fraction. **(b)** Type 2 clast of coarse fraction. **(c)** Quenched crystallization texture at high magnification of Type 2 clast.

attributed to the variation of R_m and the confining pressure (Table 7). Experiments with the high confining pressure (35.7 MPa) and R_m between 0.9 and 1.6 reached heights in excess of 1.64 m. The average MCR value for this set of experiments is 5.1% with a range of values between 4.9% and 5.4%. For R_m less than 0.7, no high confining pressure experiment recorded liftoff greater than 0.02 m due mainly to insufficient internal pressure build up. Experiments with the low confining pressure (6.8 MPa) and R_m between 0.5 and 1.5 reached heights between 0.9 m and 1.5 m. The average MCR value for this set of experiments is 3.2% for a value range of 2.9% to 3.5%. Experiments with the intermediate confining pressure (16.3 MPa) and R_m from 0.4 to 2.0, recorded liftoff heights between 0.1 m and 3.6 m. The average MCR value for this set is 2.6% with a value range between 1.0% and 5.7%.

B. Thermodynamic Conversion Ratios

Two thermodynamic models for CR calculation are based on either the assumption of adiabatic or nearly isothermal steam expansion. These models, described in Appendix B, are more poorly constrained than those described above because only measured pressure is used. The thermodynamic CRs express the maximum work that each experimental system is capable of doing, assuming that the systems are reversible and in equilibrium.

In these experimental hydrovolcanic system, the mechanical energy (work) is largely produced by the volumetric expansion of water vapor, which is a function of p_{burst}.(Fig. 17). Therefore, in a fashion similar to Equation (4), the conversion ratios for the two thermodynamic models are found by dividing the change in the adiabatic and isothermal work potentials, ΔW_a and ΔW_i respectively by the initial internal energy:

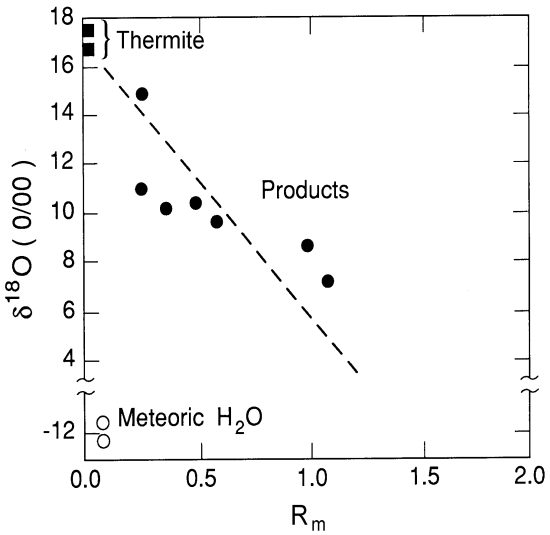

Fig. 16. Plot of $\delta^{18}O$ *vs* R_m for experiments where interaction products were recovered and analyzed. The initial thermite oxygen composition was near 17 %**0** for these experiments while the tap (meteoric) water was

near -12 %**0**. The products show a roughly linear (dashed line) decrease of $\delta^{18}O$ with increasing R_m, indicating a rapid exchange of oxygen between the hot thermite and water.

Table 7. Calculated Ejecta Velocities and Conversion Ratios*.

Experiment	R_m	*Ejecta Velocity (m/s)*	*MCR (%)*	*ACR (%)*	*ICR (%)*
P-I					
81-1	0.38	271	2.64	4.33	18.50
80-3	0.49	281	2.90	3.10	5.09
82-9	0.67	262	2.65	7.43	14.82
LOF-5	0.73	257	2.97	6.17	11.10
LOF-24	0.95	296	4.98	8.66	15.32
82-6	1.00	317	4.92	9.91	18.22
LOF-11	1.00	328	5.70	9.09	16.31
LOF-8	1.15	315	5.07	11.68	20.98
LOF-23	1.31	298	5.05	8.15	11.99
LOF-14	1.60	292	5.40	5.82	8.08
P-II					
80-4	0.62	272	2.44	5.85	12.02
80-5	0.66	166	2.45	6.28	12.79
LOF-6	0.67	261	1.71	7.43	14.82
LOF-19	0.69	269	2.49	7.49	15.34
80-1	0.96	284	3.25	5.64	7.79
LOF-1	1.00	285	3.54	6.13	8.84
82-1	1.06	252	2.86	8.32	13.21
81-2	1.20	256	3.18	7.18	10.12
LOF-22	1.20	266	2.98	6.68	9.42
LOF-13	2.00	271	4.52	7.18	9.17
P-III					
LOF-2	0.50	n.d.	n.d.	9.01	12.26
80-6	0.66	n.d.	n.d.	6.97	13.68
LOF-17	0.67	271	0.60	11.30	29.45
LOF-16	0.67	n.d.	n.d.	11.30	29.45
LOF-15	0.67	n.d.	n.d.	11.30	29.45
LOF-18	0.69	273	1.71	7.49	15.34
LOF-20	0.69	275	1.74	7.49	15.34
LOF-21	0.69	n.d.	n.d.	7.49	15.34
82-4	1.00	272	1.81	9.09	16.31
82-5	1.00	267	1.77	9.09	16.31
82-7	1.00	269	2.56	9.09	16.31
LOF-12	1.25	220	1.04	7.86	22.50
LOF-7	1.50	279	2.45	14.19	25.63

* Experiments are listed in order of increasing R_m for each pressure group. Ejecta velocities are calculated by Equation (9) with constraints of pressure records and vessel LOH. MCR, ACR, and ICR designate Mechanical [Eq. (10)], Adiabatic [Eq. (13)], and Isothermal [Eq. (15)] conversion ratio calculations, respectively. Experiments where liftoff was not recorded did not allow calculation of ejecta velocity nor MCR (n.d.); these are all grouped into P-III.

$$\mathrm{ACR} = \frac{\Delta W_a}{m_m C_m \Delta T} \quad , \tag{5}$$

$$\mathrm{ICR} = \frac{\Delta W_i}{m_m C_m \Delta T} \quad . \tag{6}$$

The calculated ICR values range from 5.1% to 29.5% and are generally twice those of the calculated ACR values (3.1% to 14.2%) for similar experiments (Table 7; Fig. 18). The difference in CR values calculated by these two models reflects the additional expansion work of the water vapor produced by heat supplied from the entrained fragments. In reality, the degree to which the approximately isothermal model is valid depends upon the size of entrained fragments and the duration of thermal contact.

The trends of three sets of conversion ratios (CR) with R_m are described by best-fit lognormal curves, illustrated in

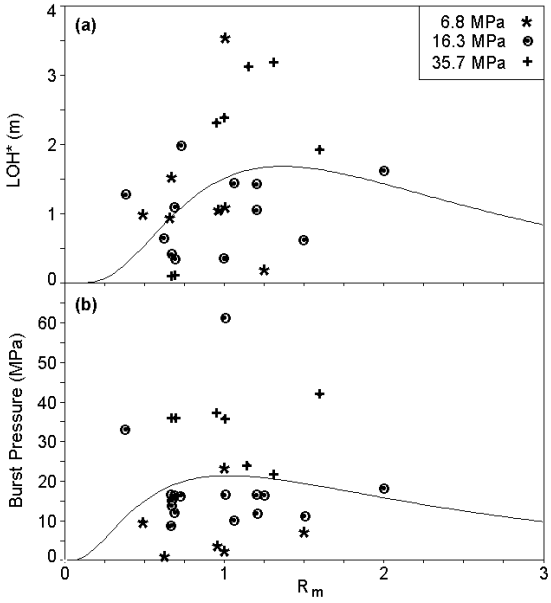

Fig. 17. Variation of (a) normalized liftoff height (LOH* = LOH/kg thermite) and (b) burst pressure (p_{burst}) with R_m for experiments at three different p_{conf}. The data for each pressure set roughly follow a lognormal dependence on R_m (average curve for all data shown) that *Wohletz* [1986] found to be a theoretical relationship between mechanical energy and water/melt mass ratio.

Figure 18. Comparing the mechanical energy conversion ratios with the two thermodynamic conversion ratios reveals that MCR does not exceed the ACR and ICR for any experiment. Only the work done by the expansion and ejection of the water-fragment mixture are considered in the MCR calculation. Other modes of mechanical energy, such as fragmentation and acoustic energy, are more accurately accounted for in the ACR and ICR models. A more likely explanation for the lower values of MCR is that the water and thermite melt did not reach thermal equilibrium prior to burst nor during post-burst expansion, a result that can be attributed to the short duration of the experimental interaction (note that the adiabatic and isothermal models assume initial thermal equilibrium). Because of the time constraints required for pre- and post-burst thermal equilibrium to occur, we consider the MCR values to be near the correct values for these experiments. The discrepancy between the MCR values and those obtained by thermodynamic considerations (ACR and ICR) reflect the degree to which these systems approached thermal equilibrium both before and after burst.

C. Ejecta Tendencies

Unfortunately, ejecta samples are very limited because of the difficulty in retaining samples considered to be representative of the populations. Previous work[21] described

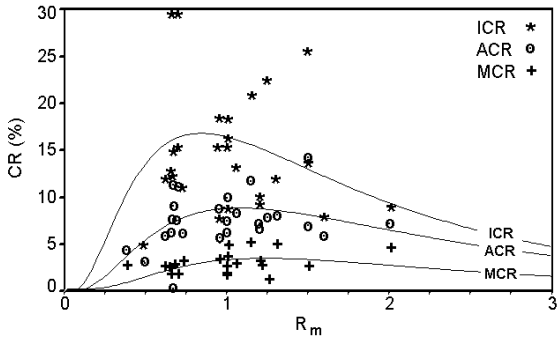

Fig. 18. Plot of conversion ratios *vs* R_m. MCR denote ratios calculated by documented mechanical energy of the vessel and the ejecta, while idealized thermodynamic ratios were calculated assuming adiabatic expansion (ACR) and approximately isothermal expansion (ICR). The theoretical curves, as described for Figure 17, show a crude correspondence to the data and are expressed as $f(R_m) = a + b \exp\{-0.5\,[\ln(R_m/c)/d]^2\}$. For this expression the constants are for MCR a = 0.01, b = 3.3, c = 1.2, and d = 0.67 (r^2 = 0.82), for ACR a = 0.073, b = 8.8 c = 1.1, and d = 0.78 (r^2 = 0.90), and for ICR a = 0.17, b = 17.0 c = 0.75, and d = 0.93 (r^2 = 0.85).

an apparent decrease in ejecta size with increasing explosive energy. Figure 19 shows, for this limited sample set, the variation of ejecta diameter with R_m with calculated MCR. Following the data trends described for variations of CR with R_m, best-fit lognormal curves show a crudely defined minimum of clast sizes near R_m = 0.8 (Fig. 19a), and the tendency for the clast diameter of the ejecta to fall

off with increasing values of MCR (Fig. 19b), as theoretically predicted by Wohletz.[24]

We also see a tendency for certain ejecta shape types to be correlated with the three main pressure groups characterized by sample shape data shown in Table 6. Figure 19 shows variations of these sparse data with R_m and MCR. The data are too few to support any trends strongly and only hint at support of the theoretically curves fit to them, which predict highest average shape factor values at R_m = 0.8 (Fig. 19c) and increasing shape factor values with increasing MCR (Fig. 19d).

V. DISCUSSION

To summarize and interpret the analytical results, the trend of mechanical energy conversion ratios (MCR) with the water to melt mass ratio R_m for the experiments within the three pressure groups is shown in Figure 20. This plot shows that the observed pressurization mode is strongly linked to the resulting conversion ratio for each experiment. Recalling that the discrepancy between the ACR and the MCR values for a given experiment estimates the degree to which the water-thermite melt interaction approached thermal equilibrium, we further assume that the

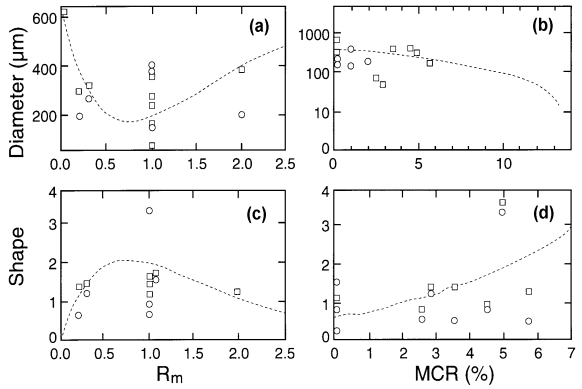

Fig. 19. **(a)** Plot of thermite ejecta average diameter determined by SEM (stars) and mean diameters by sieving (circles) *vs* R_m. Lack of data makes the curve (described in Fig. 18) a very uncertain fit. **(b)** Plot of thermite ejecta average diameter determined by SEM (stars) and mean diameters by sieving (circles) *vs* MCR. Again the best-fit curve is mostly hypothetical with too few data to support the fit. **(c)** Plot of average shape factors (stars) and their standard deviations (circles) of the thermite ejecta *vs* R_m. The curve shows a theoretical variation of shape factor. **(d)** Plot of average shape factors (stars) and their standard deviations (circles) of the thermite ejecta *vs* MCR. The curve shows the exponentially rising fit of shape factors with R_m.

pressure-time curves are records of internal pressurization events. It is apparent upon comparing Figures. 18 and 20 that the MCR values for the P-I experimental systems came closest to the calculated ACR values. The range of MCR values for P-II experiments are lower than those for P-I experiments with the same R_m. The P-III experiments have the lowest MCR values for a given R_m; hence they are the experiments that do not approach thermal equilibrium. With this result, it is possible to characterize three different heat exchange histories for these three groups of experiments; each history is characterized by a distinct variation of the functional form of the pressure-time curve. We interpret these variations in pressurization in terms of the heat exchange rate which controlled the type of vapor films formed prior to burst.

A. Superheating

When water contacts a heated surface at a temperature greater than the saturation temperature, either the temperature of water rises by equilibrium processes or it is superheated to that surface temperature.[25,26] For metallic surfaces or thermitic melt, the surface heat flux is sufficiently high to superheat water and form a thermal boundary layer at the interface.[27,28] Figure 21 demonstrates how the heat flux in the thermal boundary layer varies as a function of the surface superheat temperature. The surface superheat temperature (ΔT) is the difference between the surface temperature and the saturation temperature of water for a given pressure.[27] At a surface superheat temperature less than 320 K, water in the thermal boundary layer is in a superheated (metastable liquid) state. The heat flux through the boundary layer increases with increasing temperature because no heat energy is lost to vaporization. This region on the heat flux-temperature boiling curve is termed the nucleate boiling region and arises due to the generation of vapor bubbles above the superheated boundary layer.[27,29]

At a surface superheat temperature between 320 and 453 K, vapor nuclei form on a microscopic scale and grow until a critical size is reached. This growth results in formation of a thermal boundary layer through which vapor bubbles extend to the site where nucleation is occurring.[27,30] The rate of formation of critical-size nuclei increases exponentially with increasing temperature to a point where superheated water spontaneously vaporizes.[24] This temperature interval is coincident with the transition boiling region on the heat flux-temperature boiling curve. Transition boiling is delineated by the exponential decrease in heat flux due to latent heat consumed in forming vapor nuclei.

Vapor film boiling is established at a superheat temperature greater than 453 K, the limit of superheat (*e.g.*, the spontaneous nucleation temperature) at one atmosphere pressure. The upper surface phenomenon is complex and depends on the rate of vapor-film growth and thickness.[31,32] At higher pressures, the general shape of

the superheat boiling curve remains the same but the maximum heat flux is shifted toward lower surface superheat temperatures.[33] The heat flux in the vapor film boiling regime is not affected by pressure and so the boiling curves converge near the minimum heat flux point. However, the heat flux associated with vapor-film boiling decreases by up to a factor of 10 as the wetting angle increases (Fig. 21).

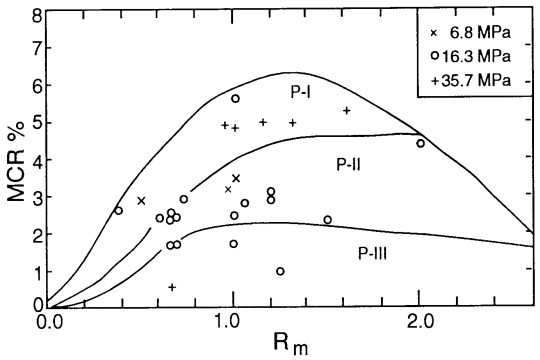

Fig. 20. Trend of mechanical conversion ratio (MCR) with the water/melt mass ratio (R_m) for experiments with different p_{conf}. Delineated field show the range of data for the experiments exhibiting pressure records of a given group. P-I experiments showed MCR values greater than those of P-II, and P-III experiments showed the lowest MCR values. This relationship strongly indicates that the mode of pressurization is linked to the mechanism of fragmentation and heat exchange for these experiments.

In the interpretations of the pressure-time curves, an melt temperature of 1000 K has been assumed based on the melting temperature of the aluminum partition. The boiling curve predicts that at a superheat temperature of 900 K, a vapor film will form at the melt surface and will act to insulate the melt from the ambient water. In order to raise the bulk temperature of water within the time span of the experimental interaction (0.8s to 15.0s), the vapor film must be destabilized. Several vapor film destabilization models have been proposed: (1) Taylor-Helmholtz instability[31,32]; (2) pulsation film boiling[32,34]; and (3) vapor film transplosion.[32,35]

B. Vapor Film Destabilization

Rayleigh-Taylor and Kelvin-Helmholtz instabilities arise when a light fluid (water vapor) accelerates into and along a dense fluid (liquid water) and produce perturbations that grow along the interface between the two. The vapor-film thickness grows steadily as the wavelength and amplitude of individual perturbations increase until their amplitude is approximately equal to 0.4 times their wavelength.[31] At that time these perturbations become unstable and detach from the film to form a vapor bubble. When the vapor bubbles detach, a gap in the vapor film is created allowing liquid to collapse onto the heated surface and vaporize instantaneously. The spacing of bubbles corresponds to the perturbation wavelength that has the maximum growth rate. Berenson[31] predicts wavelength perturbation, vapor-film thickness, and bubble growth rate as a function of density and temperature difference. The general results from Berenson's[31] calculations indicate that as the temperature difference increases from 373 to 773 K, the maximum growth rate and the maximum wavelength doubles. In addition, the effect of vapor-film velocity and thickness become more apparent at larger temperatures.

During an experimental study on vapor film boiling, Stevens and Witte[32] observed irregularities forming at the liquid-vapor interface of the vapor film that formed on the surface of a spherical mass of silver heated to temperatures between 593 to 853 K. The irregularities were vapor bubbles <1.6 mm in diameter. The growth and detachment of bubbles at the liquid-vapor interface triggered oscillations in the vapor film, which initiated pulsations normal to the surface of the sphere. After approximately 50 to 100 ms, the vapor film destabilized and pulsation boiling was established.

Pulsation boiling refers to a rhythmic growth and collapse of the vapor film normal to the heated surface. Stevens and Witte[32] found that the pulsating motion of the a water-vapor film at surface temperatures less than 623 K may be symmetric or asymmetric with an average frequency estimated at 2 kHz. As the vapor film grows, it pushes against the surrounding liquid. When maximum growth is achieved, the liquid then pushes on the film accelerating its collapse. The oscillatory behavior is caused by the difference in the rates of thermal diffusion and momentum transfer (sound speed).

Transplosion of the vapor film refers to the sudden explosion of a stable vapor film.[32] Condensation at the liquid-vapor interface results in contraction of the vapor film; as the film thins, the heat flux through it increases.[21] The explosive destruction of a vapor film occurs when a relatively smooth film condenses to a thickness corresponding to a critical heat flux. Assuming the liquid-vapor interface remains smooth and thus void of nucleation sites, conditions for superheat are favorable. Thinning of the vapor film continues until the heat flux is sufficiently high to raise the temperature of the liquid at the liquid-vapor interface above the superheated limit. At the superheated limit, water instantaneously vaporizes creating a vaporization wave that propagates out into the surrounding liquid water with concomitant expansion of the vapor film.[35] Subsequently, when the film expands to a

maximum thickness, heat flux through it decreases to the point where growth can no longer be sustained, and the film begins to condense and collapse. The above process may be repeated. It is likely that the collapse of a vapor film leading to its sudden explosion can be initiated by an external stress wave.

C. Fuel-Coolant Interactions

From experimental studies on fuel-coolant interactions, it has been shown that the initial destabilization of the liquid-vapor interface can cause roughening and fragmentation of melted surfaces. Surface tension forces are overcome by the relative motion of the fuel and coolant and pressure waves associated with film growth and collapse are present. Additional melt surface area is created by surface roughening and fragmentation, which thereby enhances the rate of heat transfer between the melt and water and further pressurizes the system. Buchanan[15] formulated a model to calculate the magnitude of a pressure wave after several events of vapor film collapse. His model involves axisymmetric film collapse and water jet penetration to deform and fragment the melt surface. A peak propagation pressure of 662 MPa was calculated for six cycles of film collapse over an elapse time of 0.21s. The kinetic energy of

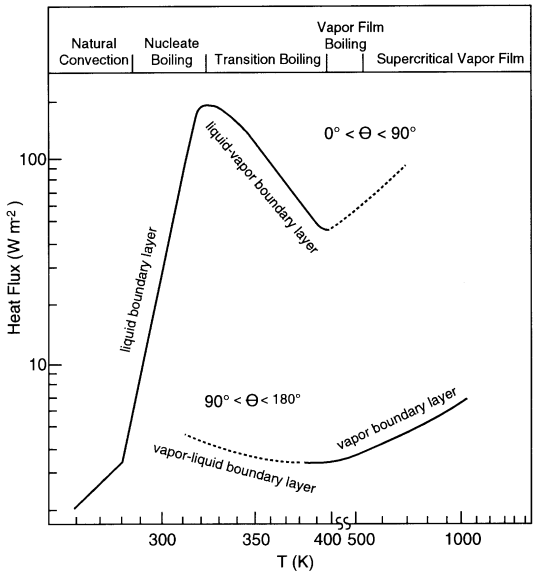

Fig. 21. Modified superheat boiling curve adapted from *Gaertne*r (1965), Moissis and *Berenson* (1963), and *Hesse* (1973), showing the variation of the rate of heat transfer (Q) through a boundary layer (*e.g.*, a heated interface such as that between magma and water) as a function of superheat temperature (ΔT). θ denotes the wetting angles; dashed lines are inferred; and solid lines are experimentally determined.

the collapse increased from 1.2×10^{-4} J to 9.8×10^{5} J and fragmented approximately 0.17 kg of melt.

Thermal fragmentation can generate pressure waves of 150 MPa propagating at 90 m/s during vapor film growth after an initial film destabilization.[21,36] This model requires Taylor instabilities that destabilize the melt surface during film collapse. The Taylor instabilities grow and detach by the acceleration of the melt surface during vapor film growth. During growth and detachment, melt fragments are mixed into the ambient water thus increasing the heat transfer and vapor-film growth rate. This process may lead to the propagation of a vaporization-wave front, as described above for the transplosion process. When the rate of expansion behind the wave front approaches the sound speed of the water-melt fragment mixture, the pressure wave behaves as a type of detonation wave.[34] The pressure driving the wave is sustained by rapid water vaporization.

D. Analysis of the Fragmentation Processes

The dominant clast types produced from several experiments are listed in Table 6. Although the number of experimental samples is limited, an interesting correlation has been observed with respect to the three pressure groups: (1) P-I experiments LOF-11 and 82-6 both produced predominantly Type 3 clasts; (2) P-II experiments 82-1, LOF-1, and LOF-13 produced two common clast types, Types 4 and 6; (3) Experiment 82-7 classified as P-III produced Types 1 and 2 clasts. Type 6 clasts are absent. Although no pressure record was obtained for 82-7, its character is so similar to that of LOF-7 that we will use the LOF-7 pressure record for interpretation. The variation in clast types observed for these three groups of experiments suggests that we are observing a consequence of the dynamic behavior of water as it is being heated by the melt during preburst mixing.

By combining the fragmentation models proposed by Wohletz[21], which describe the formation of each hydrovolcanic clast type, the sequence of events that produced the pressure histories and clast types is inferred for each pressure group. We assume the viscosity of thermite prior to significant quenching to be 100 Pa s and that it can respond to initial mixing with water by ductile or viscous deformation. With quenching below about 1000 K, the thermite melt will be deformed in a brittle fashion by the stress waves propagated by vapor expansion. The following descriptions outline our interpretation of the experimental morphologies.

1. P-I Experiments. These experiments produced primarily Type 3 clasts. The pressure histories for this group of experiments show an exponential pressure rise followed by an abrupt dynamic decompression. The ex-

ponential growth of pressure at constant volume requires an exponential rise in water temperature (hence heat flux) with time. We model this exponential rise in heat flux by assuming the heat flux is proportional to melt surface area and the melt is gradually fragmented into smaller and smaller particles. With formation of successively smaller particles the total amount of surface area for heat flux increases. If the average particle radius r decreases *linearly* with time t (i.e., $r = r_o - q\,t$, where r_o is initial melt radius and q is the rate of size decrease) and the particles have a constant combined volume, the surface area increases at a rate of $4\,\pi\,q\,r_o^3 / (r_o - q\,t)^2$, which when integrated over time appoximates an exponential rise in surface area. The gradual fragmentation of the melt can be nicely explained by vapor-film oscillation. Each collapse of the film perturbs the melt surface leading to detachment of melt fragments. Based on the observations of Stevens and Witte[32], these oscillations are expected to have a frequency of several kHz. Then several thousand pulsations, each causing a finite degree of melt fragmentation, are likely to have produced the observed exponential rise in pressure up to the point where the burst valve failed and the water explosively expanded. Where the burst occurred at pressures above the designed burst-valve limit, the pressure gauges, which were placed fairly high in the vessel, were most likely reacting in a manner not appropriate to the whole vessel. In particular, the area near the valve had sand covering it, which could have protected it from the dynamic reaction sensed by the pressure gauge.

Type 3 clasts appear to have developed by viscous deformation under tensional stress conditions created during rapid vapor film formation. These conditions are predicted by the development of Rayleigh-Taylor and Kelvin-Helmholtz instabilities. These instabilities[24] are caused by the relative motion of the vapor film along the melt surface. They perturb the melt surface and introduce additional morphological characteristics. Tiny plumes of melt rise from the surface when surface tension forces are exceeded by Rayleigh-Taylor instabilities. Kelvin-Helmholtz instabilities are induced by shear stresses that further stretch and disperse the melt surface. Because these instabilities form with a range of wavelengths and orientations, melt surfaces can become very convoluted, resulting in tortuous, high surface area fragments.

2. P-II Experiments. Types 4 and 6 clasts are common to all of these experiments with Type 5 being important in two of the samples investigated. The sequence of pressurization events shown by this group of experiments is thought to be characteristic of cyclic growth and collapse of insulating vapor films around drops of melt as the melt gradually pours into the water. As more melt contacts the water, the bulk temperature of the water increases to a point where a superheat vapor explosion occurs. The initial pressure rise is linear with time and reflects the increased temperature of vapor boundary layers on melt surfaces. When the oscillation of the upper vapor-film interface, mentioned previously, reaches a critical wavelength and amplitude, vapor bubbles detach and jets of liquid water penetrate the gap left in the film and contact melt surfaces. Upon contact with melt, liquid water will instantaneously transform to vapor if the surface temperature of the melt is above the critical point of water. The phase transformation involves a volumetric change creating an outward force that can generate convective motion within the boundary layer and enhance the destabilization of the interface. The vapor boundary layers become highly irregular in shape and thickness, which increases the number of localities where liquid water can penetrate the vapor layer and contact the melt surface. For this process the simplest behavior may be a linear increase in vapor fraction with time. Based upon the simple isothermal equation of state for water, the pressure rise should also be linear with time. During vapor film collapse, water jets penetrating the melt can further increase its fragmentation. When the bulk temperature of the water reaches the spontaneous nucleation temperature, which depends on the local pressure, water spontaneously vaporizes and can propagate a vaporization wave front that might account for the terminating pressure spike observed just prior to burst.

Type 4 clasts show strong effects of surface tension and must form when the melt is still hot enough to be very fluid. This situation is consistent with vapor films that insulate the melt. As with Type 3 clasts, melt surface instabilities both grow and detach to form spherical or elongated ribbon-like structures in response to the force of locally collapsing vapor films. This process can be enhanced when melt instabilities are sheared off by boundary layer stripping processes.[37,38] The most rapid mechanism contributing to production of Type 4 clasts occurs when compression waves associated with vapor film collapse become large enough to shatter the surface undulations produced by instabilities; this results in the production of a multitude of fine-grained fragments. When axisymmetric collapse of vapor films produces accelerations sufficient to overcome surface tension forces of fluid melt, water jets can penetrate into the melt and become partially or completely entrapped beneath the surface. The trapped water becomes superheated and expands explosively causing fragmentation of melt surfaces.

Type 5 clasts are plates that appear to be pieces of quenched crust stripped off the surface of the melt. The stripping process can be attributed to the turbulence of

vapor film oscillation, vaporization wave propagation, or Kelvin-Helmholtz instability. In this interpretation, these clasts are very similar to Type 1 clasts. Also contributing to Type 5 morphology is fragmentation of portions of the melt containing abundant, nearly coalescing vapor vesicles. Vapor vesicles are common in large (>1 cm) fragments of thermite ejecta. The vesicles form by rapid entrapment of water in still fluid melt (as with water jet penetration). Subsequent vaporization of the entrapped water and growth of vapor bubbles results in a foam that is subsequently shattered by stress waves resulting from its rapid ejection from the vessel.

Type 6 clasts are formed by the partial fusion of fine-grained fragments, such as Types 1, 4, and 5, onto the surface of a larger fragment, the core clast. The process of agglomeration requires that the melt fragments come into contact before surface temperatures fall below the solidus. The degree of fusion is a function of the surface temperature, and the size and shape of individual melt fragments.

3. P-III Experiments. Types 1 and 2 clasts dominate ejecta from these experiments, with subordinate contributions of Type 4 and 5 clasts. The pressure records of these experiments are distinguished by their parabolic increase of pressure. Oscillation of vapor films along water/melt interfaces created stress waves sufficiently strong to deform and fragment the melted surface by Taylor and Helmholtz instability. Because the overall growth of the vapor fraction likely follows a parabolic law[39] where $r \propto (D\,t)^{1/2}$, and the bulk thermal diffusivity (D) of water decreases with increasing vapor fraction, the isothermal increase in bulk pressure as a function of vapor fraction [bubble radius (r)] should be a function of the square root of time (t). This prediction is supported by the pressure histories of P-III experiments with p_{conf} being approached slowly. However, many of the P-III experiments burst before reaching p_{conf}. In these events it is likely that because of the relatively long duration of the pressure rise, the burst valve was heated sufficiently to fail prematurely.

Types 1 and 2 clasts resemble (1) shards of shattered glass or (2) clasts that are twisted and deformed with fluidal surface textures. These fragments form when stress waves propagate through the melt and produce deformation rates that exceed its bulk modulus. In this case, it is envisioned that the local temperature of the melt is near solidus and brittle fractures develop in response to thermal contraction or tensional stress waves produced by vapor film collapse. Because stress waves typically propagate faster than thermal waves, it is likely that thermal contraction only affects melt surfaces while the bulk of the melt is rapidly subjected to mechanical stresses.

In quenched portions of the melt, fractures tend to propagate at angles less than 45° to the melt surface, forming block-shaped clasts with planar to curviplanar surfaces (Type 1). Vapor film oscillation may produce turbulence that tends to spall quenched melt fragments from the surface of the molten body and expose unquenched surfaces. For portions of the melt that fragment prior to quenching, vapor turbulence can cause deformation of unquenched shards with melt surface tension promoting formation of fluidal surface textures (Type 2).

VII. CONCLUSIONS

Fuel-coolant interaction experiments in which Fe-Al thermite was mixed with H_2O were designed to quantify conversion of the molten fuel heat energy into mechanical energy. The conversion ratios (MCR) of mechanical energy were calculated from records of the vessel's motion caused by the propulsion by jets of steam and hot thermite ejecta spewed from the vessel's nozzle. The vessel's internal pressure records were also used to estimate thermodynamic work conversion ratios by idealized adiabatic (ACR) and approximately isothermal (ICR) expansion calculations. With analysis of the quenched thermite ejecta size and shape distributions, the variation in conversion ratios as a function of water/melt mass ratio (R_m) and the designed vessel confining pressure have been investigated with respect to theoretical fragmentation and heat transfer mechanisms.

The conversion ratios show a lognormal dependence on R_m and an overall increase with confining pressure. MCR values were nearly 6% at R_m near 1.0 and fall off to less than 1% as R_m becomes less or greater. Since MCR values are approximately half of corresponding ACR values, and ACR values are in turn about half of corresponding ICR values, it is likely that the experimental interactions never achieved thermal equilibrium between the water and the thermite either before or after burst. This result suggests that the duration of the experiments was not long enough to reach maximum conversion ratios. Secondly, a portion of the vapor expansion work was partitioned into melt fragmentation, and as such cannot be easily quantified by our experimental setup.

If the duration of water/melt interaction influences the amount of heat energy transmitted to the water, then larger scale interactions might produce higher conversion ratios. This conclusion is generally supported by comparisons of small, 1-gram of fuel-coolant interactions that produce conversion ratios less than 1% with those discussed here. One might conclude that volcanoes may attain very high conversion ratios of magmatic heat to explosive energy. However, the experiments tell us that

about half of the potential expansion energy goes into melt fragmentation. Hence, volcanoes no matter what size will show eruption column energies that are much less than perhaps half of that predicted by idealized thermodynamic models such as those given by Wohletz.[24]

By using the ACR curve calculated from these experiments, one can make some conservative estimates of the explosive energy (E) of hydroclastic eruptions. If the volume of magma (V_m) erupted is known and the water/magma mass ratio (R_m) is constrained by analysis of the deposits,[2,40] the estimation is

$$E = \xi_a \left(\rho_m V_m C_m \Delta T \right) \quad , \tag{7}$$

where ρ_m is the magma density, ΔT is the magma temperature minus 373 K, and $\xi_a \approx 9 \exp\{-0.5 [\ln(R_v)/0.8]^2\}$ is a simplified best-fit curve for the ACRs (expressed as fractions) found in these experiments (Fig. 18) where $R_v = 3R_m$ because thermite has approximately three times the heat content of most magmas. With E calculated, the maximum ejecta velocity ($u_{\max}$) is simply given by

$$u_{\max} = \left(\frac{2E}{\rho_m V_m} \right)^{1/2} \quad . \tag{8}$$

Given the vent diameter, the mass flux of ejecta is constrained by $u_{\max}$, and one can then estimate an eruptive column height (h_c) based on formulas for buoyant plumes[41] for the ash component. The ballistic fountain heights (h_b) for lapilli-sized ejecta is $h_b = u_{\max}^2 / 2g$.

Another conclusion based upon these experimental results is that explosive interactions can occur where p_{conf} is above the critical pressure of water. It has long been held that when interactions occurred at depths where the lithostatic or hydrostatic pressure was greater that the critical pressure explosive interaction could not happen.[42] The explosive expansion of water vapor need not occur through the two-phase liquid and vapor field. As required by observational constraints of these experiments, explosive burst occurred from preburst pressures of more than 60 MPa. The sound speed of the liquid/vapor/solids mixture determines whether expansion can occur at explosive rates.

The experimental ejecta show correlation of fragment shapes and size distributions with the observed explosive efficiencies (CR). The most explosive (highest CR) experiments produced dominantly Type 3 clasts that are characterized by moss-like, convoluted shapes of very high surface area. Intermediate CR experiments produced Type 4, 5, and 6 clasts that have spherical to drop-like shapes, plate-like to crescent-like shapes, and can be aggregates. Low CR experiments are typified by blocky, equant to tabular grains. Hydrovolcanic tephra show all these grain types,[45] but the most commonly reported ones are the Type 1 clasts, which suggests that hydrovolcanic fragmentation mechanisms may not be the result of the most efficient fuel-coolant interactions. This conclusion is very speculative because of the vast difference in scale and detailed rheological properties of most magmas and the thermite analog. Most studied hydroclasts come from relatively small volcanoes such as tuff rings and cones. We note also that the dominant experimental grain types are also a function of size fraction and that the finer fractions do show shapes that are more suggestive of higher conversion ratios. This same observation seems to exist for hydrovolcanic tephra in which finer fractions exhibit more of the Type 3, 4, and 5 clasts; in fact, samples of phreatoplinian tephra do show clast types that can be correlated to the moderate and high CR experimental tephra.[43]

Appendix A: Ejecta Velocity Calculation

The derivative form of conservation of momentum is expressed by the following equation.

$$\frac{\partial(\rho u)}{\partial t} + \nabla \cdot \left(\rho u^2 \right) = \rho g - \nabla p + K_d |\Delta u| - \nabla \cdot \tau \quad , \tag{A-1}$$

where u is the ejecta velocity, ρ is the density of the ejecta, g is the gravitational acceleration, p is the pressure, τ is the viscous stress tensor, and K_d is the drag coefficient of the ejecta moving through the vent nozzle and air at a slip velocity of Δu. Assuming the atmosphere to be at rest, the flow of the ejecta to be one-dimensional and inviscid, and negligible momentum advection, Equation (A-1) simplifies to

$$m du + u dm = mg dt - V \frac{dp}{dx} dt + K_d V u dt \quad . \tag{A-2}$$

Here $V\, dp / dx = A_n\, p(t)$ is the force accelerating the jet through the nozzle of area A_n. To solve Equation (A-2) for the ejecta velocity (u_e) with respect to the vessel velocity (u_v), we set the left-hand side of Equation (A-2) to equal the final momentum minus the initial momentum of the vessel (mu_v).

$$m du + u dm = \left[(m - dm)(u_v + du_v) + u_e dm \right] - m u_v \quad . \tag{A-3}$$

In this equation, dm represents the change in the vessel mass caused by ejection of its contents. By assuming $dm\, du_v$ is negligibly small and inserting Equation (A-3) into Equation (A-2), u_e is specified:

$$u_e \frac{dm}{m} = -u_v \frac{dm}{m} - du_v + gdt - A_n \frac{p(t)}{m} dt + V \frac{K_d}{m} u dt \quad \text{.(A-4)}$$

The last term on the right side of Equation (A-4) accounts for volumetric drag produced by tangential (K_f) and normal (K_s) forces acting on the jet surface due to relative fluid motion:

$$V K_d u = K_f u_e^2 + K_s u_e \quad , \qquad \text{(A-5)}$$

where $K_f = 0.5\, \rho_a A_j C_d$ and $K_s = 12\, \pi \mu L$, ρ_a is the density of air (1.22 kg/m^3), μ is the bulk viscosity of the jet (~0.01 Pa-s), and L is the length of the jet. A_j is the surface area of the jet, assumed to be conic in shape, and $A_j = \pi r [r + (L^2 + r^2)^{1/2}]$, where r is the radius of a cone determined by the relation r = radius of the burst valve + L/(tan 60°). After integrating Equation (A-4) and noting that $u_v \propto (2\, g\, h)^{1/2}$ where h = LOH (the maximum height reached), the result can be written as a quadratic equation with respect to the ejecta velocity (u_e):

$$\left[\frac{K_f}{m} \right] u_e^2 + \left[\frac{K_s}{m} - \ln \frac{m}{m_f} \right] u_e + \left[gt - \frac{A_n}{m} p_t - (2gh)^{1/2} \left(1 - \ln \frac{m}{m_f} \right) \right] = 0 \qquad \text{(A-6)}$$

with m being the initial mass of the vessel and its contents, and m_e being the mass ejected. The final mass m_f of the vessel is m - m_e. While the integral of pressure (p_t) can be graphically determined from pressure records, C_d is a function of u_e, adding a nonlinearity to Equation (A-6); hence, an iterative approach is required for its solution.

Appendix B: Thermodynamic Models

Thermodynamic work is expressed by the laws of thermodynamics:

$$dU = dQ + dW \quad , \qquad \text{(B-1)}$$

where the change in internal energy (dU), expressed as an exact differential, equals the sum of the changes in heat energy (dQ) and mechanical work (dW); $dU = C_v\, dT$, $dQ = C_p\, dT$, and $dW = -p\, dV$. C_v and C_p are the specific heats at constant volume and constant pressure respectively and T is temperature, p the pressure, and V the specific volume.

In the *adiabatic* model, no heat is gained or lost from the system (dQ = 0), and the work potential (dW_a) equals the change in the water's internal energy (dU) after its decompression to atmospheric conditions ($dU = -pdV$). The total work potential for this model is given by

$$\Delta W_a = m_w \left[(H_1 - p_1 V_1) - (H_2 - p_2 V_2) \right] \quad , \qquad \text{(B-2)}$$

where H is the enthalpy at the initial (1) and final (2) states. Assuming adiabatic (isentropic) expansion conditions, the final thermodynamic state of water is defined by the initial entropy (S_i) equaling the final entropy (S_f) at a pressure of 1 atm.

The approximately *isothermal* model assumes that the expanding steam stays in perfect thermal contact with the hot thermite ejecta. Here, $dW_i = dU - dQ$ and $p\, dV = dQ - dU$ where $dU = d(H - p\, dv) - C_m\, dT$. For this case the total work potential is given by

$$\Delta W_i = m_w \left[C_p \Delta T + x_1 (H_1 - p_1 V_1) - x_2 (H_2 - p_2 V_2) \right] + m_m \left[C_m \Delta T \right] \qquad \text{(B-3)}$$

where $C_m \Delta T = \Delta Q$ is the change in heat content of the melt, and x_1 and x_2 denote the initial and final steam fractions. The work (ΔW_i) of the expanding mixture is equal to the sum of the changes in internal energy and heat of the three phases (liquid water, water vapor, and melt). The model assumes that the water maintains a common temperature with the fragmented thermite while the water-fragment *mixture* expands isentropically. Because the hot entrained fragments of thermite constantly supply heat energy to the expanding water as a function of the water-to-thermite mass ratio (R_m), the steam's temperature does not fall adiabatically but approaches isothermal behavior. This approximately isothermal behavior is caused by a linear increase in the expanding-steam entropy as a function of R_m given by $dS = C_m\, dT / (R_m\, T)$. Wohletz[24] discusses in detail the calculation of the work potential (dW_i) for four possible thermodynamic pathways that high-pressure water may follow during decompression to atmospheric conditions.

These thermodynamic models for adiabatic and approximately isothermal expansions have been written in computer code for the experimental system in order to calculate the work potential of high-pressure water expanding to atmospheric pressure. The code implements the basic relationships described above, along with some additional derivations given by Wohletz[24] and tabulated thermodynamic properties of water at high pressure and temperature.[44] Pressure, specific volume, and R_m define the initial thermodynamic state of the experimental system in both models (p, V, T, S). For these calculations, designed confining pressures were used as conservative values for the initial pressure (p_1), because there were reasons why these might be more reliable than those actually measured, as discussed earlier. The initial volume of water was assumed to be equal to the size of the vessel chamber not occupied by melt or air. The initial temperature was calculated using Equation (1) of Wohletz[24], which assumed that the melt and water come to thermal equilibrium prior to burst. P-T variations in the specific heat and polytropic exponent of water were obtained from tables.

ACKNOWLEDGMENTS

We thank the support and technical personnel of the shock-wave physics group of Los Alamos National Laboratory, especially Austin Bonner, for their help in imple-

menting these experiments. Tony Heller deserves special recognition for his innovative design improvements and for maintaining an experimental schedule despite adverse conditions. Steve Self suggested that this analysis be undertaken with the goal of trying to understand the effects of fuel-coolant interaction mechanisms on ejecta size and shape characteristic. Lionel Wilson provided a thorough and helpful review. This work was done under the auspices of the U. S. Department of Energy through Laboratory Directed Research and Development funds.

REFERENCES

1. S. Thorarinsson, *Surtsey: the New Island in the North Atlantic*, 53 pp., Almenna Bokafelagid, Reykjavik, Iceland (1966).

2. M. F. Sheridan and K. H. Wohletz, "Hydrovolcanism: basic considerations and review," *J. Volcanol. Geotherm. Res.,* **17**, 1-29 (1983).

3. K. H. Wohletz and R. G. McQueen, "Experimental studies of hydromagmatic volcanism," *Explosive Volcanism: Inception, Evolution, and Hazards*, edited by F. R. Boyd, Jr., pp. 158-169, Studies in Geophysics, National Academy Press, Washington, D. C. (1984).

4. F. Barberi, J. M. Navarro, M. Rosi, R. Santacroce, and A. Sbrana, "Explosive interaction of magma with ground water: insights from xenoliths and geothermal drillings," *Rend. Soc. Ital. Mineral. Petrol.,* **43**, 1-22 (1988).

5. M. F. Sheridan and K. H. Wohletz, "Hydrovolcanic explosions: the systematics of water-tephra equilibration," Sci., **212**, 1387-1389 (1981).

6. G. Fröhlich, "Similarities and differences between stratified experiments and entrapment experiments," *Amer. Soc. Mech. Engr.*, **84-HT-19**, 1-9 (1984).

7. G. Fröhlich, "Interaction experiments between water and hot melts in entrapment and stratification configurations," *Chem. Geol.,* **62**, 137-147 (1987).

8. B. Zimanowski, V. Lorenz, and G. Fröhlich, "Experiments on phreatomagmatic explosions with silicate and carbonatite melts," *J. Volcanol. Geotherm. Res.*, **30**, 149-153 (1986).

9. B. Zimanowski, G. Fröhlich, and V. Lorenz, "Quantitative experiments on phreatomagmatic explosions," *J. Volcanol. Geotherm. Res.*, **48**, 341-358 (1991).

10. S. G. Lipset, "Explosions from molten materials and water," *Fire Tech.,* **May**, 118-126 (1966).

11. S. J. Board, C. L. Farmer, and D. H. Poole, "Fragmentation in thermal explosions," *J. Heat Mass Trans.,* **17**, 331-339 (1975).

12. L. D. Buxton and W. B. Benedict, "Steam explosion efficiency studies," *Rep. SAND79-1399, NUREG/CR-0947*, 62 pp., Sandia Natl. Lab., Albuquerque, New Mexico (1979).

13. M. L. Corradini, "Analysis and modeling of steam explosion experiments," *SAND80-2131 (NUREG/CR-2707)*, 114 pp., Sandia Natl. Lab., Albuquerque, New Mexico (1980).

14. D. E. Mitchell, and N. A. Evans, "Steam explosion experiments at intermediate scale: FITSB series," *SAND83-1057 (NUREG/CR-3983)*, 72 pp., Sandia Natl. Lab., Albuquerque, New Mexico (1986).

15. D. J. Buchanan, "A model for fuel-coolant interactions," *J. Phys. D Appl. Phys.,* **7**, 1441-1457 (1974).

16. K. H. Wohletz, "Explosive hydromagmatic volcanism," Ph. D. dissertation, 303 pp, Ariz. State Univ, Tempe, Arizona (1980).

17. Y. A. Bottinga, and D. F. Weil, "The viscosity of magmatic silicate liquids: a model for calculation," *Amer. J. Sci.,* **272**, 438-473 (1972).

18. S. A. Colgate and T. Sigurgeirsson, "Dynamic mixing of water and lava," Nature, **244**, 552-555 (1973).

19. K. H. Wohletz and M. F. Sheridan, "Martian rampart crater ejecta: experiments and analysis of melt-water interaction," *Icarus*, **56**, 15-37 (1983).

20. K. H. Wohletz, M. F. Sheridan, and W. K. Brown, "Particle size distribution and the sequential fragmentation/transport theory applied to volcanic ash," *J. Geophys. Res.,* **94**, 15,703-15,721 (1989).

21. K. H. Wohletz, "Mechanisms of hydrovolcanic pyroclast formation: grain size, scanning electron microscopy, and experimental results," *J. Volcan. Geotherm. Res.,* **17**, 31-63 (1983).

22. B. E. Taylor and K. H. Wohletz, "Oxygen isotope exchange in phreatomagmatic phenomena: experimental and natural studies," *Abs. Int'l. Volcanol. Congr.*, Aukland-Hamilton-Rotorua, New Zealand, 122 (1985).

23. B. M. Smith, "Oxygen isotope evidence for magma-groundwater interactions in early post-collapse rhyolites from the Long Valley caldera, California," Geol. Soc. Am. Abs. Progs., **20(7)**, A114 (1988).

24. K. H. Wohletz, "Explosive magma-water interactions: thermodynamics, explosion mechanisms, and field studies," *Bull. Volcan.*, **48**, 245-264 (1986).

25. R. C. Reid, "Superheated liquids," *Amer. Sci.*, **64**, 146-156 (1976).

26. H. K. Fauske, "On the mechanism of uranium dioxide-sodium explosive interactions," *Nucl. Sci. Eng.*, **51**, 95-101 (1973).

27. R. F. Gaertner, "Photographic study of nucleate pool boiling on a horizontal surface," *J. Heat Trans.*, 17-29 (1965).

28. L. C. Witte, J. E. Cox, and J. E. Bouvier, "The vapor explosion," *J. Metals*, **22**, 39-44 (1970).

29. R. Moissis and P. J. Berenson, "On the hydrodynamic transitions in nucleate boiling," *J. Heat Trans.*, 221-226 (1963).

30. K. Nishikawa, T. Fujii, *et al.*, "Experimental study of the mechanism of transition boiling heat transfer," *Bull. Japan Soc. Mech. Engr.*, **15**, 93-103 (1972).

31. P. J. Berenson, "Film boiling heat transfer from a horizontal surface," *J. Heat. Trans.*, **August**, 351-356 (1961).

32. J. W. Stevens and L. C. Witte, "Destabilization of vapor film boiling around spheres," *Intern. J. Heat Mass Trans.*, **16**, 669-678 (1973).

33. G. Hesse, "Heat transfer in nucleate boiling, maximum heat flux and transition boiling," *J. Heat Mass Trans.*, **16**, 1611-1627 (1973).

35. J. W. Stevens, "Transient film and transition boiling from a sphere," Ph. D. dissertation, Univ. of Houston, Houston, Texas (1972).

36. M. L. Corradini, "Phenomenological modeling of the triggering phase of small-scale steam explosion experiments," *Nucl. Sci. Eng.*, **78**, 154-170 (1981).

37. J. E. Shepherd and B. Sturtevant, "Rapid evaporation at the superheat limit," *J. Fluid Mech.*, **121**, 379-402 (1982).

38. B. Sturtevant and D. Frost, "Effects of ambient pressure on the instability of a liquid boiling explosively at the superheat limit," *Proc. Symposium of Fundamentals of Phase Change: Boiling and Condensation*, Amer. Soc. Mech. Eng., Winter Meeting (1984).

39. L. E. Scriven, "On the dynamics of phase growth," *Chem. Eng. Sci.*, **10**, 1-13 (1959).

40. K. H. Wohletz, "Vaporization and condensation of water during hydrovolcanic eruptions," *New Mex. Bur. Mines Min. Res. Bull.*, **131**, 296 (1989).

41. L. Wilson, R. S. J. Sparks, T. C. Huang, and N. D. Watkins, "The control of volcanic column heights by eruption energetics and dynamics," *J. Geophys. Res.*, **83**, 1829-1836 (1978).

42. V. Lorenz, "On the growth of maars and diatremes and its relevance to the formation of tuff rings," *Bull. Volcanol.*, **48**, 265-274 (1986).

43. G. Heiken and K. Wohletz, *Volcanic Ash*, University of California Press, Berkeley, California, 246 p. (1985)

44. L. Haar, J. S. Gallagher, and G. S Kell, *NBS/NRC Steam Tables*, 320 pp., Hemisphere Publishing, New York (1984).